



# Coupled magneto-mechanical growth in hyperelastic materials: Surface patterns modulation and shape control in bio-inspired structures

Zhanfeng Li <sup>a</sup>, Yafei Wang <sup>c</sup>, Zuodong Wang <sup>a</sup>, Chennakesava Kadapa <sup>d</sup> \*, Mokarram Hossain <sup>e</sup> \*, Xiaohu Yao <sup>a,b,\*\*</sup>, Jiong Wang <sup>a,b</sup> \*\*

<sup>a</sup> School of Civil Engineering and Transportation, South China University of Technology, Guangzhou, 510640, China

<sup>b</sup> State Key Laboratory of Subtropical Building and Urban Science, South China University of Technology, Guangzhou, 510640, China

<sup>c</sup> Department of Mechanical and Energy Engineering, Southern University of Science and Technology, Shenzhen, 518055, China

<sup>d</sup> School of Computing, Engineering and the Built Environment, Edinburgh Napier University, Edinburgh, EH10 5DT, United Kingdom

<sup>e</sup> Zienkiewicz Institute for Modelling, Data and AI, Faculty of Science and Engineering, Swansea University, Swansea, SA1 8EN, United Kingdom

## ARTICLE INFO

### Keywords:

Magneto-elasticity  
Differential growth  
Finite element analysis  
Surface pattern evolution  
Shape control

## ABSTRACT

Magneto-mechanical coupling in the growth of soft materials presents challenges due to the complex interactions between magnetic fields, mechanical forces, and growth-induced deformations. While growth modeling has been extensively studied, integrating magnetic stimuli into growth processes remains underexplored. In this work, we develop a 3D governing system for capturing the coupled magneto-mechanical growth behaviors of soft materials. Based on the governing system, we propose a finite element framework, where the robustness and accuracy of the proposed framework are demonstrated through numerical simulations, including the uniaxial loading of a circular tube, a mesh convergence study, and surface pattern evolution. We also conduct experiments on surface pattern modulation in magneto-active soft materials. Specifically, we fabricate film-substrate samples and apply growth-induced instabilities combined with external magnetic fields to generate tunable surface patterns. To demonstrate the capabilities of our method, we apply our numerical framework to mimic the biological morphogenesis, such as the inversion process of the algal genus *Volvox*. Our study shows that integrating magneto-mechanical coupling with growth effects allows for flexible control over surface patterns, significantly enhancing the adaptability and responsiveness of soft materials. This work paves the way for innovative designs of adaptive and programmable soft materials, with potential applications in soft robotics, biomimetic structures, and tissue engineering.

## 1. Introduction

Growth of soft materials refers to changes in the mass or volume of soft material samples under specific conditions (Ambrosi et al., 2011). These changes may arise from biological factors (e.g., tissue swelling due to injury) or physical factors (e.g., hydrogel expansion via water absorption or pneumatic stretching of rubber). The concept of growth extends beyond biological contexts and

\* Corresponding author.

\*\* Corresponding authors at: School of Civil Engineering and Transportation, South China University of Technology, Guangzhou, 510640, China.

E-mail addresses: [C.Kadapa@napier.ac.uk](mailto:C.Kadapa@napier.ac.uk) (C. Kadapa), [Mokarram.Hossain@Swansea.ac.uk](mailto:Mokarram.Hossain@Swansea.ac.uk) (M. Hossain), [yaoxh@scut.edu.cn](mailto:yaoxh@scut.edu.cn) (X. Yao), [ctjwang@scut.edu.cn](mailto:ctjwang@scut.edu.cn) (J. Wang).

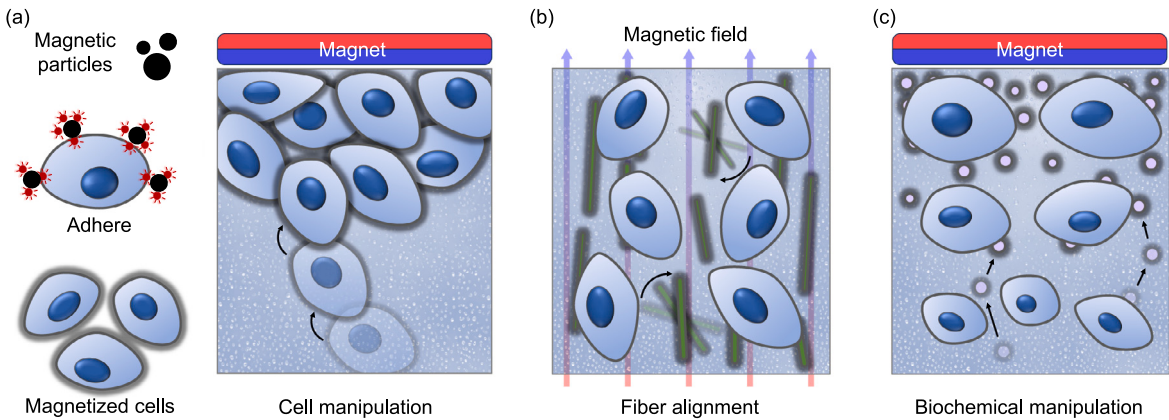


**Fig. 1.** Magnetic stimulation as a versatile tool in tissue engineering: (a) spatial positioning of magnetized cells (Abdel Fattah et al., 2023); (b) alignment of extracellular matrix fibers (Hiraki et al., 2021); (c) regulation of growth factor distribution (Li et al., 2018).

plays a crucial role in engineering. In engineering, growth refers to the controlled expansion or contraction of materials to achieve desired shapes and functionalities, facilitating advancements in areas such as soft robotics, smart materials, and adaptive structures. Although the factors inducing growth-related deformations are diverse, the resulting effects can generally be attributed to the pre-strain applied by the internal growth field (growth function) to local material points. Soft materials often undergo differential growth, characterized by non-uniform or incompatible growth fields. Such incompatibilities can lead to complex mechanical responses, including surface pattern formation (van Rees et al., 2017; Liu et al., 2024b) and alterations in internal structure (Ambrosi et al., 2019). The study of growth-induced deformations and morphological evolution in soft materials, encompassing theoretical modeling, analytical analysis, and numerical simulations, has become one of the most active research areas in soft material mechanics (Li et al., 2012; Rausch and Kuhl, 2014; Goriely, 2017; Liu et al., 2024a).

Growth in soft materials frequently couples with chemical (Xue et al., 2016; Franze, 2020), diffusive (Chockalingam and Cohen, 2024), or electrical stimuli (Du et al., 2020), which further complicate the mechanical responses of biological tissues. In particular, magneto-mechanical growth, where magnetic fields interact with mechanical forces to modulate growth behavior, has garnered significant interest (Gomez-Cruz et al., 2024). Biological experiments have demonstrated that growth phenomena can be manipulated through the application of magnetic fields (Armstrong and Stevens, 2020). To regulate cell behavior and enhance tissue regeneration, recent studies have integrated magnetic particles with external fields to generate mechanical forces at the cellular level. Fig. 1 illustrates three key applications of magnetic stimulation in tissue engineering: (a) magnetic nanoparticles can be adhered to cell membranes, generating magnetized cells with spatial positioning capabilities through external magnetic fields (Abdel Fattah et al., 2023); (b) Hiraki et al. (2021) developed magnetically alignable fibers to control tissue engineering environments, guiding morphogenesis, mechanical load distribution, and cell migration; (c) Li et al. (2018) introduced a platform for controlling growth factor gradients in biomaterials.

The mechanism of magneto-mechanical growth involves the use of magnetic fields to generate mechanical forces that stimulate cellular activities. By embedding magnetic particles in scaffolds or cells, external magnetic fields apply forces to cell membranes, activating mechano-transduction pathways. These forces trigger changes in the cytoskeleton, promoting processes such as cell proliferation, migration, and differentiation. The non-invasive nature of magnetic stimulation offers a safer alternative for modulating cellular processes.

Inspired by biological adaptation mechanisms, researchers have engineered materials incorporating magnetic particles that exhibit growth-like behaviors, such as magnetically responsive hydrogels (Li et al., 2013; Tang et al., 2019) and magnetic bioinks (Vítková et al., 2023). Notable examples include 3D-printed pollen-inspired microrobots with magnetically driven motion (Lee et al., 2023) and biodegradable bilayer microgrippers responsive to thermal and magnetic stimuli (Kobayashi et al., 2019). These materials combine magnetic particles with elastic materials to achieve programmable deformations via magnetic and growth fields, offering advantages in soft robotics and actuators. These magneto-active soft materials are created by embedding magnetic particles into growth-responsive elastic matrices, enabling programmable deformations through superimposed magnetic and growth fields. Unlike conventional magneto-active materials, they exhibit unique magnetic actuation and volumetric changes under non-contact control. This dual responsiveness proves particularly advantageous in inaccessible environments (e.g., biomedical implants) or extreme conditions (e.g., space robotics), where traditional mechanical interventions are impractical. Their spatiotemporal programmability drives innovations in adaptive actuators and soft robotic systems (Lee et al., 2023; Moreno-Mateos et al., 2023; Khalid et al., 2024).

Theoretical models for growth and magneto-active materials address two key aspects:

- **growth effects:** By introducing a growth tensor, we can represent the growth field within the sample (Ben Amar and Goriely, 2005; Goriely and Ben Amar, 2005; Yavari, 2010). To account for both the material's elastic response and the growth-induced changes, the total deformation gradient tensor is decomposed into a product of the elastic deformation tensor and the growth tensor (Kondrakov and Nikitin, 1987; Rodriguez et al., 1994; Sadik and Yavari, 2017).

- **magnetoelastic coupling:** Total energy density is usually decomposed into magnetic and elastic parts (Dorfmann and Ogden, 2004). For the magnetic component, Zhao et al. (2019) first proposed a constitutive model for hard magneto-active elastomers (ideal hard-magnetic soft materials) within the framework of finite strain theory. The model was validated using several test cases involving thin-walled structures subjected to pure magnetic loading (Kim et al., 2018; Zhao et al., 2019). However, a numerical framework for isotropic and incompressible hard magneto-active elastomers proposed by Mukherjee et al. (2021) revealed that magnetization depends solely on the rotational component of the deformation gradient (Mukherjee et al., 2021). To address these findings, Yan et al. (2023) proposed a modified magnetic potential energy function in which the total deformation gradient is replaced by the rotation tensor. Subsequent analysis by Danas and Reis (2024) demonstrated that the fully dissipative model developed by Mukherjee et al. (2021) can be reduced to the energetic model of Yan et al. (2023), but not to the earlier model by Zhao et al. (2019). Recent advances include microstructural models accounting for dipole interactions (Garcia-Gonzalez and Hossain, 2021) and symmetric stress formulations (Dorfmann and Ogden, 2024). For the elastic part, commonly used hyperelastic constitutive models, such as neo-Hookean, Mooney–Rivlin, and Gent models, can be employed (Lu et al., 2024). Since the elastic deformation of some typical soft material samples is generally incompressible, corresponding incompressibility constraints should be introduced into the 3D governing equations.

Numerical methods such as traditional finite element analysis (Firouzi and Amabili, 2024), isogeometric analysis (Wang et al., 2020), and molecular dynamics (Cleary and Hancock, 2021) have been employed to simulate growth. Growth effects are often incorporated through the multiplicative decomposition of the deformation gradient (Himpel et al., 2005; Kadapa et al., 2021). In addition to purely growth-induced deformation, numerical simulations that account for coupled growth effects have also been developed. For instance, Hong et al. (2008) proposed a thermodynamic theory to describe the swelling and diffusion effects in hydrogels, laying a foundation for further developments in this area. Chester et al. (2015) developed an ABAQUS user subroutine (UEL) to simulate the coupled mechanical-diffusion response of hydrogels. Hu et al. (2024) explored the swelling deformation of thermally responsive, magnetic-particle-embedded hydrogels under varied temperatures and magnetic fields. Previous work by the authors addressed the electro-mechanically coupled growth of soft materials (Li et al., 2023a). However, magneto-mechanical growth coupling remains underexplored.

Developing continuum mechanics-based models that can consider mechanical, magnetic, and growth-induced responses is still challenging. Although some analytical solutions can be derived from the 3D governing equations, they are often limited to simplified boundary conditions and constitutive models, rendering them inadequate for capturing the nonlinear behavior encountered in real-world applications. Thus, a theoretical model and the corresponding numerical framework for magneto-mechanical coupled growth is indispensable for capturing the complex interactions between mechanical forces, magnetic fields, and growth effects in soft materials.

This study aims to establish a comprehensive theoretical and numerical framework to model the coupled magneto-mechanical growth behavior in soft materials. Specifically, the objectives are: (1) to propose a theoretical framework that integrates both magneto-mechanical responses and growth effects in soft materials; (2) to develop a computationally efficient numerical method capable of handling complex geometries and large deformations; (3) to validate the model through experiments, demonstrating its applicability in practical contexts such as tissue engineering and biomimetic robotics. This work bridges biological and engineering perspectives, offering insights into tissue development and enabling advanced control over magneto-active polymers. Potential applications include studying surface pattern evolution, crease formation, and instability phenomena.

The paper is structured as follows: Section 2 presents governing equations for nonlinear magnetomechanics with growth. Section 3 details the finite element formulation and numerical implementation. Section 4 validates the framework through analytical solutions and convergence studies. Section 5 investigates magnetic field effects on surface patterning. Section 6 applies the framework to analyze Volvox inversion. Conclusions and future directions are discussed in Section 7.

## 2. Governing equations for nonlinear magnetomechanics with growth effects

In this section, the equations governing the coupled magneto-mechanical growth behavior of hyperelastic materials are discussed.

### 2.1. Kinematics and the modeling of growth effects

We consider a homogeneous magneto-elastic solid situated in 3D Euclidean space  $\mathcal{R}^3$ . The reference configuration of the solid body is denoted as  $\mathcal{K}_r$ . By defining an orthogonal frame  $\{O; \mathbf{e}_1, \mathbf{e}_2, \mathbf{e}_3\}$ , the position vector of a material point in  $\mathcal{K}_r$  is represented as  $\mathbf{X} = X_i \mathbf{e}_i$ . Here,  $\mathbf{e}_i$  ( $i = 1, 2, 3$ ) denotes the orthonormal basis vectors in the reference configuration. Due to external forces, magnetic stimuli, growth effects, or a combination of all, the solid deforms from  $\mathcal{K}_r$  to the current configuration  $\mathcal{K}_t$ . The position vector of a material point in  $\mathcal{K}_t$  is denoted by  $\mathbf{x} = x_i \mathbf{e}_i$ . The displacement field of the body is defined as

$$\mathbf{u}(\mathbf{X}) = \mathbf{x}(\mathbf{X}) - \mathbf{X}. \quad (1)$$

Then, the deformation gradient tensor  $\mathbb{F}$  can be calculated through

$$\mathbb{F} = \frac{\partial \mathbf{x}}{\partial \mathbf{X}} = \mathbb{I} + \frac{\partial \mathbf{u}}{\partial \mathbf{X}}, \quad (2)$$

where  $\mathbb{I} = \delta_{ij} \mathbf{e}_i \otimes \mathbf{e}_j = \mathbf{e}_i \otimes \mathbf{e}_i$  is the second-order identity tensor.

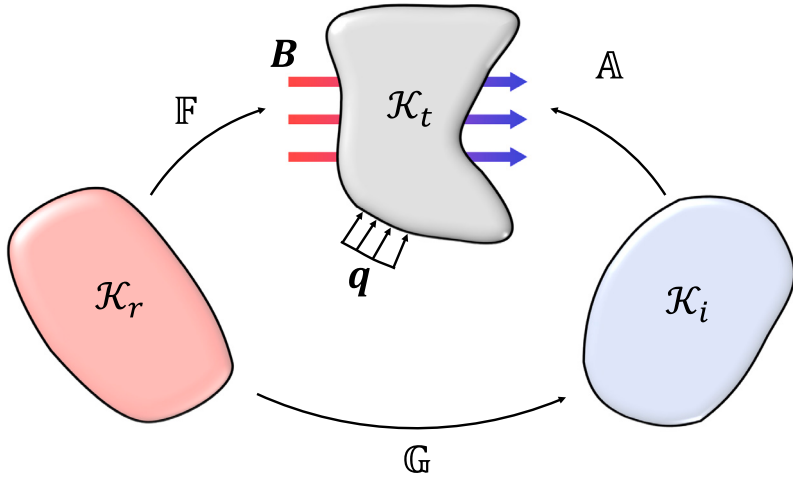


Fig. 2. Decomposition of the deformation gradient  $\mathbb{F}$ .

Following the foundational assumptions of growth theory (Kondrakov and Nikitin, 1987; Rodriguez et al., 1994; Ben Amar and Goriely, 2005), the deformation gradient tensor  $\mathbb{F}$  is decomposed into

$$\mathbb{F} = \mathbb{A}\mathbb{G}, \quad (3)$$

where  $\mathbb{A}$  is the elastic deformation tensor and  $\mathbb{G}$  is the growth tensor. Based on this decomposition (3), the deformation of the sample can be understood in two sequential steps (cf. Fig. 2): first, a transformation from the reference configuration  $\mathcal{K}_r$  to the stress-free intermediate configuration  $\mathcal{K}_i$  under pure growth condition; then, an elastic deformation from  $\mathcal{K}_i$  to the current configuration  $\mathcal{K}_t$ . Due to the incompatibility of the growth field, material points in  $\mathcal{K}_i$  may be discontinuous or overlapping (Skalak et al., 1996). Therefore, the intermediate configuration is virtual rather than physical.

Assuming that the growth rate is significantly slower than the elastic response of the material, the distribution of the growth tensor  $\mathbb{G}$  is considered time-independent. Since the elastic energy of a growing isotropic material depends solely on the symmetric part of the growth tensor (Goriely, 2017), it is beneficial to constrain the growth tensor to a symmetric form,  $\mathbb{G} = \lambda_{ij}\mathbf{e}_i \otimes \mathbf{e}_j$ , where  $\mathbb{G} = \mathbb{G}^T$ . The components  $\lambda_{ij}(X)$  represent the growth functions along and between these basis directions, varying spatially as functions of the position vector  $X$ .

## 2.2. Magnetostatics and constitutive model

Hard-magnetic soft composites are created by embedding hard-magnetic particles, such as neodymium-iron-boron (NdFeB), within a soft, elastic matrix. Once magnetically saturated, these particles retain a high remanent magnetization, represented by the magnetization density  $\mathbf{M}(X)$  (per unit reference volume). Unlike soft magnetic materials, hard-magnetic particles exhibit significant resistance to demagnetization, attributed to their intrinsic coercivity. When subjected to an external magnetic field  $\mathbf{H}_a$ , these composites experience a magnetic torque due to the interaction between the remanent magnetization and the external field. This torque generates internal stresses within the matrix, causing reversible deformations of the sample. Accompanying the deformation of the sample, the magnetization vector has the Euclidean form  $\mathbf{m}$ , which is related to  $\mathbf{M}$  through the following equation

$$\mathbf{m} = J^{-1}\mathbb{F}\mathbf{M}, \quad (4)$$

where  $J = \det \mathbb{F}$ . This formulation ensures that the total number of magnetic particles is preserved during volumetric changes. For instance, when a hydrogel swells in water, the particle density decreases due to volume expansion ( $J > 1$ ), consistent with experimental observations of magneto-active materials. Furthermore, Eq. (4) is grounded in continuum mechanics and theoretically applicable to describing the kinematics of magnetization vector.

Due to the magnetization of the magnetic particles, a self-induced(or stimulated) magnetic field  $\mathbf{H}_s$  is triggered within and around the sample. We denote the scalar potential of this stimulated magnetic field as  $\phi(\mathbf{x}(X)) = \Phi(X)$ . Then, the magnetic field  $\mathbf{H}_s$  can be expressed as

$$\mathbf{H}_s = -\text{grad } \phi = -\mathbb{F}^{-T} \text{Grad } \Phi. \quad (5)$$

The applied magnetic field  $\mathbf{H}_a$  is externally specified at every spatial position  $\mathbf{x}$  and remains unchanged regardless of the sample's deformation. While the stimulated magnetic field  $\mathbf{H}_s$  arises from the magnetization and is influenced by the deformation of the sample. As the sample undergoes deformation, the magnetization vector  $\mathbf{m}$  changes accordingly, which in turn alters the stimulated field  $\mathbf{H}_s$ . This interaction creates a coupling between the mechanical deformation and the internal magnetic responses of the material. By treating  $\mathbf{H}_a$  and  $\mathbf{H}_s$  separately, the model effectively distinguishes between the external magnetic influences and the internal magnetoelastic interactions that arise from the material's deformation.

To describe the magnetic response of hard-magnetic soft materials, we adopt the constitutive model proposed by Brown (1966). The magnetic potential energy per unit reference volume is expressed as

$$\Psi_m(\mathbf{x}, \phi) = -\mu_0 J (\mathbf{H}_a + \mathbf{H}_s) \cdot \mathbf{m} - \frac{1}{2} \mu_0 J \mathbf{H}_s \cdot \mathbf{H}_s, \quad (6)$$

where  $\mu_0$  is the magnetic permeability of free space, and the magnetization vector  $\mathbf{m}$  is defined within the sample. In fact, Eq. (6) comprises the magnetostatic energy associated with  $\mathbf{H}_s$  and the Zeeman energy associated with  $\mathbf{H}_a$ , which are expressed in the following integral forms, respectively:

$$\begin{aligned} \int_{\mathcal{K}} \Psi_m^s dV &= \int_{\mathcal{K}_r} -\mu_0 J \left( \mathbf{H}_s \cdot \mathbf{m} + \frac{1}{2} \mathbf{H}_s \cdot \mathbf{H}_s \right) dV + \int_{\mathcal{K}_a} -\frac{1}{2} \mu_0 J \mathbf{H}_s \cdot \mathbf{H}_s dV, \\ \int_{\mathcal{K}} \Psi_m^z dV &= \int_{\mathcal{K}_r} -\mu_0 J \mathbf{H}_a \cdot \mathbf{m} dV. \end{aligned} \quad (7)$$

Here,  $\mathcal{K} = \mathcal{K}_r + \mathcal{K}_a$  represents the entire 3D space, while  $\mathcal{K}_a$  denotes the free space. To facilitate the definition of Lagrangian quantities in the free space, we assume a fictitious extension of the spatial position vector field  $\mathbf{x}(\mathbf{X})$  from the sample region into the surrounding space (Toupin, 1956). This extension allows for a consistent mathematical formulation of the energies across both the sample and free space regions. It should be noted that, in the absence of stimulated magnetic field  $\mathbf{H}_s$ , the magnetic potential energy function Eq. (6) reduces to the ideal hard-magnetic soft material model proposed by Zhao et al. (2019). That is,

$$\Psi_m = -\mu_0 J \mathbf{H}_a \cdot \mathbf{m} = -\mathbf{F} \mathbf{M} \cdot \mathbf{B}_a, \quad (8)$$

where the applied magnetic flux density  $\mathbf{B}_a = \mu_0 \mathbf{H}_a$ .

Zhao's model has demonstrated good agreement with experimental results under specific loading conditions. Although it has been widely adopted for its simplicity and computational efficiency, it does not account for the effects arising from the self-induced magnetic field  $\mathbf{H}_s$ , which can become significant in cases of strong magnetization or very soft matrix. In contrast, the present model incorporates the self-induced magnetic field  $\mathbf{H}_s$ , providing a more comprehensive framework for analyzing magnetoelastic interactions. In Sections 4 and 5, we will compare the two models by conducting a series of simulations under varying magnetic field strengths and material stiffnesses. Specifically, we aim to evaluate the predictive accuracy of Zhao's model against our proposed model in scenarios where  $\mathbf{H}_s$  plays a critical role. Furthermore, we will assess the computational efficiency of both models to show the trade-offs between simplicity and accuracy.

To describe the elastic response of materials incorporating growth effects, the elastic strain energy function is defined as

$$\Psi_e(\mathbb{F}, \mathbb{G}) = J_G \Psi_0(\mathbb{A}) = J_G \Psi_0(\mathbb{F} \mathbb{G}^{-1}), \quad (9)$$

where  $J_G = \text{Det } \mathbb{G}$ . Eq. (9) provides flexibility in choosing the hyperelastic model, allowing  $\Psi_0$  to represent various constitutive models such as neo-Hookean, Mooney–Rivlin, Gent, Ogden, etc. Hossain and Steinmann (2013), Mihai et al. (2017).

In soft materials such as biological tissues and polymeric gels, elastic deformations are typically isochoric. This condition can be mathematically expressed through the following constraint equation:

$$\mathcal{R}(\mathbb{F}, \mathbb{G}) = J_G (J_A - 1) = 0, \quad (10)$$

where  $J_A = \text{Det } \mathbb{A}$ . The nominal stress tensor  $\mathbb{S}$  for an incompressible hyperelastic material can then be calculated through the constitutive relation:

$$\mathbb{S} = \frac{\partial \Psi_e(\mathbb{F}, \mathbb{G})}{\partial \mathbb{F}} + p \frac{\partial \mathcal{R}(\mathbb{F}, \mathbb{G})}{\partial \mathbb{F}} = J_G \mathbb{G}^{-1} \left( \frac{\partial \Psi_0(\mathbb{A})}{\partial \mathbb{A}} + p(\mathbf{X}) \frac{\partial R_0(\mathbb{A})}{\partial \mathbb{A}} \right), \quad (11)$$

where  $p(\mathbf{X})$  is the Lagrange multiplier associated with the incompressibility constraint (10).

To model truly incompressible hyperelastic materials within the finite strain framework, the elastic component of the deformation gradient tensor, denoted as  $\mathbb{A}$ , is decomposed into volumetric and deviatoric parts (for detailed explanations, see Ogden, 1997; Bonet and Wood, 2008). This decomposition is expressed as

$$\mathbb{A} = \mathbb{A}_{\text{vol}} \mathbb{A}_{\text{dev}}, \quad (12)$$

where

$$\mathbb{A}_{\text{vol}} = J_A^{1/3} \mathbb{I}, \quad \mathbb{A}_{\text{dev}} = J_A^{-1/3} \mathbb{A}. \quad (13)$$

Based on the above definitions, the modified elastic deformation gradient tensor and the right Cauchy–Green tensor are defined as

$$\text{modified elastic deformation gradient, } \bar{\mathbb{A}} = \mathbb{A}_{\text{dev}} \quad (14)$$

$$\text{modified right Cauchy–Green deformation tensor, } \bar{\mathbb{C}} = \mathbb{A}_{\text{dev}}^T \mathbb{A}_{\text{dev}}. \quad (15)$$

Generally, the total potential energy for the magneto-active elastomers is divided into three parts: a magneto-mechanical coupling term  $\Psi_m$ , a deviatoric elastic part  $\Psi_{e,\text{dev}}$ , and a volumetric elastic part  $\Psi_{e,\text{vol}}$ . This decomposition is expressed as

$$\begin{aligned} \Psi &= \Psi_m(\mathbb{F}, \mathbf{B}_a) + \Psi_e(\mathbb{A}) \\ &= \Psi_m(\mathbb{F}, \mathbf{B}_a) + \Psi_{e,\text{dev}}(\bar{\mathbb{A}}) + \Psi_{e,\text{vol}}(J_A). \end{aligned} \quad (16)$$

For nearly incompressible materials, various forms of the volumetric energy function  $\Psi_{e,\text{vol}}$  have been utilized to accurately describe their behavior (refer to Table 1 in [Kadapa and Hossain, 2022](#) for detailed examples). In scenarios where the material is perfectly incompressible, the volumetric energy term  $\Psi_{e,\text{vol}}$  becomes negligible. To capture the behavior of perfectly incompressible material, the total potential energy is given as

$$\Psi = \Psi_m(\mathbb{F}, \mathbf{B}_a) + \Psi_{e,\text{dev}}(\bar{\mathbb{A}}) + p\mathcal{R}(\mathbb{F}, \mathbb{G}), \quad (17)$$

where  $p\mathcal{R}(\mathbb{F}, \mathbb{G})$  is the function for imposing the incompressibility constraint [\(10\)](#).

Overall, by considering the energy  $\Psi_m$ ,  $\Psi_e$ , incompressibility and external loads, we can write the total energy functional for truly incompressible magneto-active elastomers as

$$\Pi(\mathbf{x}, \phi, p; \mathbf{X}) = \int_{\mathcal{K}} (\Psi_m + \Psi_{e,\text{dev}} + p\mathcal{R}(\mathbb{F}, \mathbb{G})) \, dV - \Pi_{\text{ext}}, \quad (18)$$

where  $dV$  is the differential volume in the reference configuration. The energy contribution from external forces,  $\Pi_{\text{ext}}$ , is given by

$$\Pi_{\text{ext}} = \int_{\mathcal{K}_r} \mathbf{u} \cdot \mathbf{f}_0 \, dV + \int_{\partial\mathcal{K}_r} \mathbf{u} \cdot \mathbf{t}_0 \, dA, \quad (19)$$

where  $\mathbf{u} = \mathbf{x} - \mathbf{X}$  denotes displacement vector,  $dA$  is the differential area in the reference configuration,  $\mathbf{f}_0$  is the body force per unit volume in  $\mathcal{K}_r$ ,  $\mathbf{t}_0$  is the traction force per unit undeformed area, and  $\partial\mathcal{K}_r$  is the boundary region of the sample.

### 2.3. 3D governing system

The total energy functional  $\Pi$  depends on the independent variables magnetic potential, position vector, and hydrostatic pressure. To ensure that the magnetic sample attains an equilibrium state, the first variations of  $\Pi$  with respect to these independent variables must vanish. From these variational conditions, the three-dimensional (3D) governing equations can be derived. Following our recent work ([Wang et al., 2025](#)), the results of the variational calculations are presented below.

First, consider the variation with respect to the magnetic scalar potential. Although  $\Phi$  and  $\phi$  represent the same scalar potential in different configurations, we will adopt  $\Phi$  as the independent variable for clarity in the following variation calculations. The variation of  $\Pi$  with respect to  $\Phi$  is given by:

$$\begin{aligned} \delta_\phi \Pi &= \int_{\mathcal{K}_r} [\mu_0 \mathbf{M} \cdot \text{Grad}(\delta\Phi) - \mu_0 J (\mathbb{C}^{-1} \text{Grad} \Phi) \cdot (\text{Grad}(\delta\Phi))] \, dV \\ &\quad - \int_{\mathcal{K}_a} \mu_0 J (\mathbb{C}^{-1} \text{Grad} \Phi) \cdot (\text{Grad}(\delta\Phi)) \, dV \\ &= \int_{\mathcal{K}_r} \mu_0 [\text{Div}((\mathbf{M} - (J\mathbb{C}^{-1} \text{Grad} \Phi)) \delta\Phi) - \text{Div}(\mathbf{M} - J\mathbb{C}^{-1} \text{Grad} \Phi) \delta\Phi] \, dV \\ &\quad - \int_{\mathcal{K}_a} \mu_0 [\text{Div}((J\mathbb{C}^{-1} \text{Grad} \Phi) \delta\Phi) - \text{Div}(J\mathbb{C}^{-1} \text{Grad} \Phi) \delta\Phi] \, dV. \end{aligned} \quad (20)$$

To facilitate derivations, we introduce the Lagrangian form of the stimulated magnetic induction  $\mathbf{B}_L$  as follows:

$$\mathbf{B}_L = \begin{cases} \mu_0 (\mathbf{M} - (J\mathbb{C}^{-1} \text{Grad} \Phi)) = \mu_0 J \mathbb{F}^{-1} (\mathbf{m} + \mathbf{H}_s), & \text{in } \mathcal{K}_r, \\ -\mu_0 J \mathbb{C}^{-1} \text{Grad} \Phi = \mu_0 J \mathbb{F}^{-1} \mathbf{H}_s, & \text{in } \mathcal{K}_a. \end{cases} \quad (21)$$

Using Eq. [\(21\)](#) and applying the Gauss divergence theorem, Eq. [\(20\)](#) simplifies to:

$$\begin{aligned} \delta_\phi \Pi &= \int_{\mathcal{K}_r} -\text{Div} \mathbf{B}_L \delta\Phi \, dV + \int_{\mathcal{K}_a} -\text{Div} \mathbf{B}_L \delta\Phi \, dV \\ &\quad + \int_{\partial\mathcal{K}_r} (\mathbf{B}_L \cdot \mathbf{N}) \delta\Phi \, dV + \int_{\partial\mathcal{K}_a} (\mathbf{B}_L \cdot (-\mathbf{N})) \delta\Phi \, dV \\ &= \int_{\mathcal{K}_r} -\text{Div} \mathbf{B}_L \delta\Phi \, dV + \int_{\mathcal{K}_a} -\text{Div} \mathbf{B}_L \delta\Phi \, dV \\ &\quad - \int_{\partial\mathcal{K}_r} ((\mathbf{B}_L^o - \mathbf{B}_L^i) \cdot \mathbf{N}) \delta\Phi \, dA + \int_{\partial\mathcal{K}_a^\infty} (\mathbf{B}_L \cdot \mathbf{N}) \delta\Phi \, dA \end{aligned} \quad (22)$$

where  $\mathbf{N}$  denotes the outward unit normal vector on the boundary  $\partial\mathcal{K}_r$  of sample, and the superscripts  $o$  and  $i$  represent the values of the variables on the outer and inner sides of the interface, respectively. The boundary  $\partial\mathcal{K}_a$  represents the interface between the sample and the surrounding free space, and  $\partial\mathcal{K}_a^\infty$  represents the boundary of the free space at infinity. The magnetic potential  $\Phi$  must be regular at  $\partial\mathcal{K}_a^\infty$ . Additionally, the conditions governing the orders of  $\delta\Phi$  and  $\mathbf{B}_L$  are  $\delta\Phi \sim 1/\|\mathbf{X}\|$  and  $\mathbf{B}_L \sim 1/\|\mathbf{X}\|^2$  as  $\|\mathbf{X}\| \rightarrow \infty$ , respectively. Thus, the integral over  $\partial\mathcal{K}_a^\infty$  in Eq. [\(22\)](#) vanishes. In the equilibrium state, the variation equation satisfies  $\delta_\phi \Pi = 0$ . Considering the arbitrariness of  $\delta\Phi$ , we obtain the following magnetic field equation:

$$\begin{cases} \text{Div} \mathbf{B}_L = 0, & \text{in } \mathcal{K}_r \cup \mathcal{K}_a, \\ (\mathbf{B}_L^o - \mathbf{B}_L^i) \cdot \mathbf{N} = 0, & \text{on } \partial\mathcal{K}_r. \end{cases} \quad (23)$$

Second, consider the variation of  $\Pi$  with respect to  $\mathbf{x}$ :

$$\begin{aligned}\delta_{\mathbf{x}} \Pi = & \int_{\mathcal{K}_r} \text{tr} [(\mathbb{S} - \mu_0 (\mathbf{M} \otimes \mathbf{H}_a) + \mathbb{Q}) \text{Grad}(\delta \mathbf{x})] dV + \int_{\mathcal{K}_a} \text{tr} [\mathbb{Q} \text{Grad}(\delta \mathbf{x})] dV \\ & - \int_{\mathcal{K}_r} \mu_0 [(\text{grad} \mathbf{H}_a)^T \mathbb{F} \mathbf{M}] \cdot \delta \mathbf{x} dV - \int_{\mathcal{K}_r} \delta_{\mathbf{x}} \cdot \mathbf{f}_0 dV - \int_{\partial \mathcal{K}_r} \delta_{\mathbf{x}} \cdot \mathbf{t}_0 dA,\end{aligned}\quad (24)$$

where the quantity  $\mathbb{Q}$  is introduced to streamline the derivations:

$$\mathbb{Q} = -\frac{\mu_0 J}{2} (\mathbf{H}_s \cdot \mathbf{H}_s) \mathbb{F}^{-1} + \mu_0 J \mathbb{F}^{-1} (\mathbf{H}_s \otimes \mathbf{H}_s). \quad (25)$$

By applying the Gauss divergence theorem, Eq. (24) can be written as

$$\begin{aligned}\delta_{\mathbf{x}} \Pi = & - \int_{\mathcal{K}_r} \left[ \text{Div} (\mathbb{S} - \mu_0 (\mathbf{M} \otimes \mathbf{H}_a) + \mathbb{Q}) + \mu_0 ((\text{grad} \mathbf{H}_a)^T \mathbb{F} \mathbf{M}) + \mathbf{f}_0 \right] \cdot \delta \mathbf{x} dV \\ & + \int_{\partial \mathcal{K}_r} \left[ (\mathbb{S} - \mu_0 (\mathbf{M} \otimes \mathbf{H}_a) + \mathbb{Q})^T \mathbf{N} - \mathbf{t}_0 \right] \cdot \delta \mathbf{x} dA \\ & - \int_{\mathcal{K}_a} \text{Div} \mathbb{Q} \cdot \delta \mathbf{x} dV + \int_{\partial \mathcal{K}_a} [\mathbb{Q}^T (-\mathbf{N})] \cdot \delta \mathbf{x} dA.\end{aligned}\quad (26)$$

Across a surface of the body, the applied magnetic field  $\mathbf{H}_a$  is supposed to be continuous, while the stimulated magnetic field  $\mathbf{H}_s$  and the magnetization vector  $\mathbf{m}$  may have discontinuities. In the absence of surface currents,  $\mathbf{H}_s$  should satisfy the condition (Bustamante et al., 2008)

$$\mathbf{H}_s^o - \mathbf{H}_s^i = (\mathbf{n} \cdot \mathbf{m}) \mathbf{n}, \quad (27)$$

where  $\mathbf{n} = \mathbb{F}^{-T} \mathbf{N}$  denotes the unit outward normal vector on the interface  $\partial \mathcal{K}_r$ . By using Eqs. (23) and (27), Eq. (26) can be rewritten as:

$$\begin{aligned}\delta_{\mathbf{x}} \Pi = & - \int_{\mathcal{K}_r} \left[ \text{Div} (\mathbb{S} - \mu_0 (\mathbf{M} \otimes \mathbf{H}_a) + \mathbb{Q}) + \mu_0 ((\text{grad} \mathbf{H}_a)^T \mathbb{F} \mathbf{M}) + \mathbf{f}_0 \right] \cdot \delta \mathbf{x} dV \\ & + \int_{\partial \mathcal{K}_r} \left[ \mathbb{S}^T \mathbf{N} - \mu_0 (\mathbf{M} \cdot \mathbf{N}) \left( \mathbf{H}_a + \frac{\mathbf{H}_s^o + \mathbf{H}_s^i}{2} \right) - \mathbf{t}_0 \right] \cdot \delta \mathbf{x} dA,\end{aligned}\quad (28)$$

where an assumption that the second-order derivatives of  $\phi$  are continuous has been made. By considering the arbitrariness of  $\delta \mathbf{x}$  in the variation equation  $\delta_{\mathbf{x}} \Pi = 0$ , we obtain the following magneto-mechanical equilibrium equation:

$$\begin{cases} \text{Div} (\mathbb{S} - \mu_0 (\mathbf{M} \otimes \mathbf{H}_a) + \mathbb{Q}) + \mu_0 ((\text{grad} \mathbf{H}_a)^T \mathbb{F} \mathbf{M}) = -\mathbf{f}_0, & \text{in } \mathcal{K}_r, \\ \mathbb{S}^T \mathbf{N} - \mu_0 (\mathbf{M} \cdot \mathbf{N}) \left( \mathbf{H}_a + \frac{\mathbf{H}_s^o + \mathbf{H}_s^i}{2} \right) = \mathbf{t}_0, & \text{on } \partial \mathcal{K}_r. \end{cases} \quad (29)$$

To obtain the effective Cauchy stress  $\hat{\sigma}$ , we further rewrite Eq. (29)<sub>1</sub> into the Eulerian form. The terms to the left of the equal sign can be modified as

$$\begin{aligned}& J \text{div} \left[ \sigma - \frac{1}{2} \mu_0 [(\mathbf{H}_a + \mathbf{H}_s) \cdot (\mathbf{H}_a + \mathbf{H}_s) - \mathbf{H}_a \cdot \mathbf{H}_a - 2 \mathbf{H}_a \cdot \mathbf{H}_s] \mathbb{I} \right] \\ & + J \text{div} [\mu_0 ((\mathbf{H}_a + \mathbf{H}_s) \otimes (\mathbf{H}_a + \mathbf{H}_s) - \mathbf{H}_a \otimes \mathbf{H}_s - \mathbf{H}_s \otimes \mathbf{H}_a - \mathbf{H}_a \otimes \mathbf{H}_a)] \\ & - J \mu_0 [\text{div}(\mathbf{m}) \mathbf{H}_a + \text{grad}(\mathbf{H}_a) \mathbf{m}] + \mu_0 J (\text{grad} \mathbf{H}_a)^T \mathbf{m} \\ & = J \text{div} \left[ \sigma - \frac{1}{2} \mu_0 [(\mathbf{H}_a + \mathbf{H}_s) \cdot (\mathbf{H}_a + \mathbf{H}_s) \mathbb{I} + ((\mathbf{H}_a + \mathbf{H}_s) \otimes (\mathbf{H}_a + \mathbf{H}_s))] \right] \\ & - J \mu_0 [\text{div}(\mathbf{H}_a) (\mathbf{H}_s + \mathbf{H}_a) + \text{div}(\mathbf{H}_s + \mathbf{M}) \mathbf{H}_a],\end{aligned}\quad (30)$$

where  $\sigma = J^{-1} \mathbb{F} \mathbb{S}$ . According to Eq. (23)<sub>1</sub>, and the fact that  $\text{div} \mathbf{H}_a = 0$ , the mechanical governing equation Eq. (29)<sub>1</sub> can be rewritten as

$$\text{div} \hat{\sigma} = -\mathbf{f}, \text{ in } \mathcal{K}_r. \quad (31)$$

The effective Cauchy stress  $\hat{\sigma}$  is defined as the sum of the Cauchy stress  $\sigma$  and the symmetric Maxwell stress  $\sigma_m$ :

$$\begin{aligned}\hat{\sigma} &= \sigma + \sigma_m, \\ \sigma_m &= -\frac{1}{2} \mu_0 [(\mathbf{H}_a + \mathbf{H}_s) \cdot (\mathbf{H}_a + \mathbf{H}_s) \mathbb{I} + ((\mathbf{H}_a + \mathbf{H}_s) \otimes (\mathbf{H}_a + \mathbf{H}_s))].\end{aligned}\quad (32)$$

In the absence of currents, Eq. (31) is consistent with the governing equations presented in Rahmati et al. (2023), which is based on a nonlinear theoretical framework for modeling the magnetoelectric property of hard magnetic soft electret materials.

Third, we consider the variation with respect to the Lagrange multiplier  $p$ , which is associated with the incompressibility constraint:

$$\delta_p \Pi = \int_{\mathcal{K}_r} \mathcal{R}(\mathbb{F}, \mathbb{G}) \delta p dV, \quad (33)$$

Considering the arbitrariness of  $\delta p$  in the variation equation  $\delta_p \Pi = 0$ , we obtain the incompressibility constraint Eq. (10).

Combining the results from the variations with respect to  $\Phi$ ,  $x$ , and  $p$ , we yield the 3D governing system for the magneto-mechanical growth solid:

$$\begin{cases} \text{Div} (\mathbb{S} - \mu_0 (\mathbf{M} \otimes \mathbf{H}_a) + \mathbb{Q}) + \mu_0 \left( (\text{grad} \mathbf{H}_a)^T \mathbb{F} \mathbf{M} \right) = -\mathbf{f}_0, & \text{in } \mathcal{K}_r, \\ \text{Div} \mathbf{B}_L = 0, & \text{in } \mathcal{K}_r \cup \mathcal{K}_a, \\ \mathcal{R}(\mathbb{F}, \mathbb{G}) = 0, & \text{in } \mathcal{K}_r, \\ \mathbb{S}^T \mathbf{N} - \mu_0 (\mathbf{M} \cdot \mathbf{N}) \left( \mathbf{H}_a + \frac{\mathbf{H}_s^o + \mathbf{H}_s^i}{2} \right) = \mathbf{t}_0, & \text{on } \partial \mathcal{K}_r, \\ (\mathbf{B}_L^o - \mathbf{B}_L^i) \cdot \mathbf{N} = 0, & \text{on } \partial \mathcal{K}_r, \\ \mathbf{u} = \mathbf{u}_0, & \text{on } \partial \mathcal{K}_u^{\text{Dirichlet}}, \\ \phi = \phi_0, & \text{on } \partial \mathcal{K}_\phi^{\text{Dirichlet}}, \end{cases} \quad (34)$$

where  $\partial \mathcal{K}_u^{\text{Dirichlet}}$  and  $\partial \mathcal{K}_\phi^{\text{Dirichlet}}$  denotes the boundary region applied with displacement  $\mathbf{u}_0$  and potential  $\phi_0$ . The mechanical equilibrium Eq. (34)<sub>1</sub>, the magnetic field Eq. (34)<sub>2</sub>, the elastic incompressible constraint (34)<sub>3</sub>, along with the boundary conditions (34)<sub>4</sub> ~ (34)<sub>7</sub>, constitute the 3D governing system of the solid, which contains the unknowns  $\mathbf{u}$ ,  $\Phi$  and  $p$ .

### Remarks.

- In our model, the growth tensor  $\mathbb{G}(\mathbf{X})$  is defined as an intrinsic material property independent of external magnetic fields. However, growth-induced deformation introduces an indirect magneto-mechanical coupling through geometric mediation. The deformation alters the spatial configuration of the material, which subsequently modifies both the magnetization orientation and the surrounding magnetic field distribution.
- The growth theory employed in this study treats growth as pre-strain, enabling the model to accommodate complex scenarios such as anisotropic and non-uniform growth and geometric reconstructions. In contrast, modeling growth as initial pre-stress neglects the intermediate configuration  $\mathcal{K}_i$ , limiting its applicability to more intricate phenomena like material remodeling. Additionally, treating growth as pre-strain inherently captures physical features of the growth process, such as volume expansion. While pre-stress and pre-strain can serve as interchangeable loading variables in certain contexts, the implementation of pre-strain is notably more straightforward in numerical simulations and experimental setups. In Section 5, we utilized pre-strain to simulate growth effects for experimental convenience; however, this approach is merely an approximation of the grown configuration and does not fully represent the growth mechanism as described by finite growth theory. For scenarios involving time-dependent, inhomogeneous, or anisotropic growth, the growth theory offers a more accurate and scalable prediction of the system's response.

### 3. Mixed finite element framework

To simulate material behavior influenced by mechanical forces, magnetic fields, and growth effects, this section introduces a finite element framework with the following main steps: (1) discretization of the unknown variables  $\mathbf{u}$ ,  $\phi$  and  $p$ ; (2) derivation of the element stiffness matrix; (3) implementation through the ABAQUS subroutine UEL.

We choose the mixed formulation because it effectively handles the incompressibility constraint that arises in many material simulations, such as those involving soft tissues, rubber-like materials, and other hyperelastic materials. The mixed formulation decouples the displacement and pressure, allowing for accurate treatment of both deviatoric and volumetric components of deformation. This approach avoids issues such as volumetric locking, improves pressure accuracy, ensures numerical stability, and applies efficiently to a wide range of material regimes, from compressible to fully incompressible.

Since we are only interested in the incompressible (Poisson's ratio  $\nu$  is 0.5) or quasi-incompressible ( $0.45 \leq \nu < 0.5$ ) elastic deformations in this work, we adopt the perturbed Lagrangian form as used in Kadapa and Hossain (2022) instead of the generalized mixed formulation used for computational growth (Kadapa et al., 2021). The total energy functional  $\Pi$  is then expressed as

$$\Pi(\mathbf{x}, \phi, p; \mathbf{X}) = \int_{\mathcal{K}_r} (\Psi_m + \Psi_{e,\text{dev}} + \Psi_{e,\text{vol}} + \Psi_{\text{PL}}) \, dV - \Pi_{\text{ext}}, \quad (35)$$

where  $\Psi_{\text{PL}}$  represents the function enforcing the incompressibility constraint (10) using the perturbed Lagrangian method. Specifically,  $\Psi_{\text{PL}}$  is defined as

$$\Psi_{\text{PL}} = p J_G (J_A - 1) - J_G \frac{p^2}{2\kappa} \quad (36)$$

where  $\kappa$  is the bulk modulus of the material. In the truly incompressible case, i.e., when  $\nu = 0.5$ , or  $\kappa = \infty$ , both  $\Psi_{e,\text{vol}}$  and the term  $p^2/(2\kappa)$  vanish.

### 3.1. Discretization of the unknown variables

For the finite element discretization, we take the approximations for displacement  $\mathbf{u}$ , magnetic potential  $\phi$  and pressure  $p$  as

$$\mathbf{u} = \mathbf{N}_u \bar{\mathbf{u}}, \quad \phi = \mathbf{N}_\phi \bar{\phi}, \quad \text{and} \quad p = \mathbf{N}_p \bar{p}, \quad (37)$$

where  $\bar{\mathbf{u}}$ ,  $\bar{\phi}$  and  $\bar{p}$  are the nodal degrees of freedom (DOF) for displacement, potential and pressure, respectively. The element basis functions  $\mathbf{N}_u$ ,  $\mathbf{N}_\phi$  and  $\mathbf{N}_p$  for displacement and pressure are given by

$$\mathbf{N}_u = \begin{bmatrix} 1 N_u & 0 & 0 & \dots & {}^{nu} N_u & 0 & 0 \\ 0 & 1 N_u & 0 & \dots & 0 & {}^{nu} N_u & 0 \\ 0 & 0 & 1 N_u & \dots & 0 & 0 & {}^{nu} N_u \end{bmatrix}, \quad (38a)$$

$$\mathbf{N}_\phi = [{}^1 N_\phi \quad {}^2 N_\phi \quad \dots \quad {}^{n\phi} N_\phi], \quad (38b)$$

$$\mathbf{N}_p = [{}^1 N_p \quad {}^2 N_p \quad \dots \quad {}^{np} N_p], \quad (38c)$$

where  $nu$ ,  $n\phi$  and  $np$  denote the number of basis functions for nodal DOF. With these approximations, the first variations of the solution variables become

$$\delta \mathbf{u} = \mathbf{N}_u \delta \bar{\mathbf{u}}, \quad \delta \phi = \mathbf{N}_\phi \delta \bar{\phi}, \quad \text{and} \quad \delta p = \mathbf{N}_p \delta \bar{p}. \quad (39)$$

For an individual element, the divergence and gradient operations are introduced below. The gradient of the displacement field is represented by

$$\nabla_x \mathbf{u} = u_{i,j} = \left[ \frac{\partial u_x}{\partial x} \quad \frac{\partial u_y}{\partial x} \quad \frac{\partial u_z}{\partial x} \quad \frac{\partial u_x}{\partial y} \quad \frac{\partial u_y}{\partial y} \quad \frac{\partial u_z}{\partial y} \quad \frac{\partial u_x}{\partial z} \quad \frac{\partial u_y}{\partial z} \quad \frac{\partial u_z}{\partial z} \right]^T = \mathbf{G}_u \bar{\mathbf{u}}, \quad (40)$$

where  $\mathbf{G}_u$  is the gradient-displacement matrix. Similarly, the gradient of the magnetic potential in the current configuration is given by

$$\nabla_x \phi = \phi_{,i} = \left[ \frac{\partial \phi}{\partial x} \quad \frac{\partial \phi}{\partial y} \quad \frac{\partial \phi}{\partial z} \right]^T = \mathbf{G}_\phi \bar{\phi}, \quad (41)$$

where  $\mathbf{G}_\phi$  is the gradient-potential matrix.

To express the divergence of the displacement in vector form, we introduce a divergence-displacement matrix  $\mathbf{D}_u$  as

$$\nabla_x \cdot \mathbf{u} = u_{i,i} = \frac{\partial u_x}{\partial x} + \frac{\partial u_y}{\partial y} + \frac{\partial u_z}{\partial z} = \mathbf{D}_u \bar{\mathbf{u}}. \quad (42)$$

Details of the above formulations can be found in Kadapa et al. (2021), Li et al. (2023a).

By substituting (39) into the first variation of  $\Pi$  given in Eqs. (26), (22) and (33), the resulting semi-discrete equations for the magneto-mechanical growth problem with a mixed formulation can be written as

$$\begin{aligned} \mathbf{F}_u^{\text{int}} - \mathbf{F}_u^{\text{ext}} &= \mathbf{0}, \\ \mathbf{F}_\phi^{\text{int}} &= \mathbf{0}, \\ \mathbf{F}_p^{\text{int}} &= \mathbf{0}, \end{aligned} \quad (43)$$

where  $\mathbf{F}_u^{\text{int}}$ ,  $\mathbf{F}_\phi^{\text{int}}$  and  $\mathbf{F}_p^{\text{int}}$  are the internal force vectors for displacement, magnetic potential and pressure, respectively.  $\mathbf{F}_u^{\text{ext}}$  is the vector of external forces. These vectors are given as

$$\begin{aligned} \mathbf{F}_u^{\text{int}} &= \int_{\mathcal{K}_t} \mathbf{G}_u^T \hat{\sigma} \, dv, \\ \mathbf{F}_\phi^{\text{int}} &= \int_{\mathcal{K}_t} \mathbf{G}_\phi^T \mu_0 (\mathbf{m} + \mathbf{H}_s) \, dv, \\ \mathbf{F}_p^{\text{int}} &= \int_{\mathcal{K}_t} \mathbf{N}_p^T J_A^{-1} \left( J_A - 1 - \frac{p}{\kappa} \right) \, dv, \\ \mathbf{F}_u^{\text{ext}} &= \int_{\mathcal{K}_r} -\mathbf{N}_u^T \mathbf{f}_0 \, dV + \int_{\partial \mathcal{K}_r} \mathbf{N}_u^T \mathbf{t}_0 \, dA. \end{aligned} \quad (44)$$

For the ease of computer implementation of the finite element formulation, the effective Cauchy stress  $\hat{\sigma}$  is written as a column vector

$$\hat{\sigma} = \hat{\sigma}_{ij} = [\hat{\sigma}_{11} \quad \hat{\sigma}_{21} \quad \hat{\sigma}_{31} \quad \hat{\sigma}_{12} \quad \hat{\sigma}_{22} \quad \hat{\sigma}_{32} \quad \hat{\sigma}_{13} \quad \hat{\sigma}_{23} \quad \hat{\sigma}_{33}]^T. \quad (45)$$

### 3.2. Newton–Raphson scheme and the element stiffness matrix

The coupled nonlinear Eqs. (43) are solved using an incremental iterative approach. The subscripts  $n$  and  $n + 1$  denote the previously converged and current load steps, respectively. The displacement, magnetic potential, and pressure at the  $n$ th converged load step are represented by  $\mathbf{u}_n$  and  $\phi_n$ ,  $\mathbf{p}_n$ , respectively. The corresponding variables at the current load step are computed as

$$\begin{aligned}\mathbf{u}_{n+1} &= \mathbf{u}_n + \Delta\mathbf{u}, \\ \phi_{n+1} &= \phi_n + \Delta\phi, \\ \mathbf{p}_{n+1} &= \mathbf{p}_n + \Delta\mathbf{p},\end{aligned}\tag{46}$$

where  $\Delta\mathbf{u}$ ,  $\Delta\phi$ , and  $\Delta\mathbf{p}$  represent the load step increments from step  $n$  to  $n + 1$ . In our simulation, the growth tensor  $\mathbb{G}$  is considered as an input variable, which is updated at each load step. By adopting the Newton–Raphson scheme, the solution variables involved in the coupled nonlinear Eqs. (43) are solved iteratively at each load step. The superscripts  $k$  and  $k + 1$  denote the previous and current iterations, respectively. With iterative increments denoted by  $\bar{\Delta}\mathbf{u}$ ,  $\bar{\Delta}\phi$  and  $\bar{\Delta}\mathbf{p}$ , the variables at the current iteration are expressed as:

$$\begin{aligned}\mathbf{u}_{n+1}^{(k+1)} &= \mathbf{u}_n + \Delta\mathbf{u}^{(k+1)} = \mathbf{u}_n + \Delta\mathbf{u}^{(k)} + \bar{\Delta}\mathbf{u} = \mathbf{u}_{n+1}^{(k)} + \bar{\Delta}\mathbf{u}, \\ \phi_{n+1}^{(k+1)} &= \phi_n + \Delta\phi^{(k+1)} = \phi_n + \Delta\phi^{(k)} + \bar{\Delta}\phi = \phi_{n+1}^{(k)} + \bar{\Delta}\phi, \\ \mathbf{p}_{n+1}^{(k+1)} &= \mathbf{p}_n + \Delta\mathbf{p}^{(k+1)} = \mathbf{p}_n + \Delta\mathbf{p}^{(k)} + \bar{\Delta}\mathbf{p} = \mathbf{p}_{n+1}^{(k)} + \bar{\Delta}\mathbf{p},\end{aligned}\tag{47}$$

where  $k$  ranges from 1 to the maximum iteration count  $k_{\max}$ .

In order to solve the coupled nonlinear Eqs. (43) using the Newton–Raphson scheme, we need to linearize  $\delta\mathcal{H}$ . By taking the second variation  $d(\cdot)$  of  $\mathcal{H}$ , we have

$$\begin{aligned}d(\delta\mathcal{H}) &= \int_{\mathcal{K}_t} (\delta u_{i,j} \mathbb{e}_{ijkl} du_{k,l} + \delta u_{i,j} \mathbb{P}_{ijk} d\phi_{,k} + \delta \phi_{,i} \hat{\mathbb{P}}_{ijk} du_{j,k} + \delta \phi_{,i} \mathbb{d}_{ij} d\phi_{,j}) dv \\ &\quad + \int_{\mathcal{K}_t} \left( \delta p du_{i,i} + \delta u_{k,k} dp - \delta p \frac{J_G}{\kappa J} dp \right) dv,\end{aligned}\tag{48}$$

where  $\mathbb{e}_{ijkl}$  is the fourth-order material tangent tensor,  $\mathbb{P}_{ijk}$  and  $\hat{\mathbb{P}}_{ijk}$  are the third-order coupling tensors,  $\mathbb{d}_{ij}$  is the magnetic permeability tensor, and they are given in [Appendix A](#).

By substituting the corresponding finite element approximations into (48), we obtain the following discrete matrix system for increments  $\bar{\Delta}\mathbf{u}$ ,  $\bar{\Delta}\phi$  and  $\bar{\Delta}\mathbf{p}$  at the  $(k + 1)^{\text{th}}$  iteration:

$$\begin{bmatrix} \mathbf{K}_{uu} & \mathbf{K}_{u\phi} & \mathbf{K}_{up} \\ \mathbf{K}_{\phi u} & \mathbf{K}_{\phi\phi} & \mathbf{0} \\ \mathbf{K}_{pu} & \mathbf{0} & \mathbf{K}_{pp} \end{bmatrix} \begin{Bmatrix} \bar{\Delta}\mathbf{u} \\ \bar{\Delta}\phi \\ \bar{\Delta}\mathbf{p} \end{Bmatrix} = - \begin{Bmatrix} \mathbf{R}_u \\ \mathbf{R}_\phi \\ \mathbf{R}_p \end{Bmatrix},\tag{49}$$

where the components of the element matrix are defined as:

$$\begin{aligned}\mathbf{K}_{uu} &= \int_{\mathcal{K}_t} \mathbf{G}_u^T \mathbb{e} \mathbf{G}_u dv, \\ \mathbf{K}_{u\phi} &= \int_{\mathcal{K}_t} \mathbf{G}_u^T \mathbb{P}_{ijk} \mathbf{G}_\phi dv = \mathbf{K}_{\phi u}^T, \\ \mathbf{K}_{up} &= \int_{\mathcal{K}_t} \mathbf{D}_u^T \mathbf{N}_p dv = \mathbf{K}_{pu}^T, \\ \mathbf{K}_{\phi\phi} &= \int_{\mathcal{K}_t} \mathbf{G}_\phi^T \mathbb{d}_{ij} \mathbf{G}_\phi dv, \\ \mathbf{K}_{pp} &= - \int_{\mathcal{K}_t} \mathbf{N}_p^T \mathbf{N}_p \frac{J_G}{\kappa J} dv.\end{aligned}\tag{50}$$

$\mathbf{R}_u$ ,  $\mathbf{R}_\phi$  and  $\mathbf{R}_p$  denote the residuals, which are the differences between the internal and external force vectors:

$$\begin{aligned}\mathbf{R}_u &= \mathbf{F}^{\text{int}}(\mathbf{u}_{n+1}^{(k)}, \phi_{n+1}^{(k)}, \mathbf{p}_{n+1}^{(k)}) - \mathbf{F}^{\text{ext}}|_{n+1}, \\ \mathbf{R}_\phi &= \mathbf{F}^{\text{int}}(\mathbf{u}_{n+1}^{(k)}, \phi_{n+1}^{(k)}, \mathbf{p}_{n+1}^{(k)}), \\ \mathbf{R}_p &= \mathbf{F}^{\text{int}}(\mathbf{u}_{n+1}^{(k)}, \phi_{n+1}^{(k)}, \mathbf{p}_{n+1}^{(k)}).\end{aligned}\tag{51}$$

### 3.3. Magneto body immersed in free space

In the finite element model, we need to account for the surrounding free space to capture the effect caused by  $\mathbf{H}_s$ . For variables in the free space, we are usually more concerned with the distribution of the magnetic potential rather than the displacement field in the free space. It raises the question of how to treat displacements in a region that, physically, is purely magnetic and should not sustain appreciable mechanical stresses. Incorrect modeling of the free space domain's displacement field can inflate the computational cost, introduce artificial boundary effects, and potentially degrade numerical stability or accuracy. In practice, at least three approaches are commonly employed to address this issue:

- Modeling free space as a soft elastic medium. One assigns a low elastic modulus to the free space domain and solves for both the displacement and the magnetic potential throughout the entire computational domain. However, a large number of additional elements must be used to mesh the free space, increasing computational costs, particularly in 3D problems. Even if the elastic modulus of the free space is very low, the presence of a nonzero stiffness can induce unexpected mechanical interactions along the interface between the magnetizable body and the free space. Hence, this method is often relegated to preliminary or purely qualitative analyses where computational efficiency and high-fidelity results are not the primary concern.
- Staggered updating of free space displacements. A more refined idea, as exemplified in the work of Pelteret et al. (2016), is to decouple the displacement field in the free space from that in the magneto-active body through a staggered solution strategy. Specifically, displacements in the body are computed first by assuming that there is no motion in the free space. Once the body's displacement is determined, a virtual displacement field in the surrounding free space is updated to prevent mesh interpenetration. This approach allows the free space mesh to "follow" the body without introducing large or physically irrelevant stresses. However, for problems involving large deformations or strongly coupled magneto-mechanical effects, the staggered procedure may require many iterations and can suffer from convergence difficulties.
- Nonlocal multi-point constraint (MPC) approach. In this approach, a linear constraint is applied to each node in the free space  $\mathcal{K}_a$  relative to the displacement degrees of freedom at the magneto-active body's boundary  $\partial\mathcal{K}_r$ . Every node in the free space is constrained to move linearly based on the displacements at its nearest node on the body's boundary. As a result, the free space "follows" the deformation of the body without needing to resolve the displacement field. Through this MPC constraint, the mechanical stiffness of free space is effectively eliminated, and the global stiffness matrix remains well-conditioned.

To implement this MPC method, we first need to pair each node in the free space with its nearest counterpart on the boundary of the body. This pairing can be achieved using a nearest-neighbor search algorithm, such as the `Nearest` function in `Mathematica`. Next, following the work of Rambausek et al. (2022), we define a distance coefficient for each pair of nodes. Specifically, the distance coefficient, denoted as  $d_i^{(n)}$ , is given by the following equation:

$$d_i^{(n)} = 1 - \frac{|\mathbf{X}_i^{(n)}|_{\partial\mathcal{K}_r} - \mathbf{X}_i^{(n)}|_{\mathcal{K}_a}|}{0.5L_a}, \quad (52)$$

where  $n$  is the index of the paired nodes,  $L_a$  represents the length of the free space domain, and the subscript  $i$  denotes the coordinates index (ranging from 1 to 3 in 3D space). In fact,  $L_a$  can be chosen to be any value as long as the condition  $d_i^{(n)} > 0$  is satisfied. Once the distance coefficients are computed, we apply a constraint to each node pair, linking the node on the boundary of the body to its corresponding node in the free space, which is expressed as:

$$u_i^{(n)}|_{\mathcal{K}_a} = d_i^{(n)} u_i^{(n)}|_{\partial\mathcal{K}_r}. \quad (53)$$

By enforcing this constraint, the displacement DOFs of the free space nodes are effectively eliminated. It greatly reduces computational costs and ensures that the convergence rate and accuracy of the magnetomechanical solutions are maintained. The implementation of this approach can be efficiently handled using a direct elimination technique, such as the built-in `*EQUATION` command in ABAQUS, which allows for the elimination of these displacement DOFs.

### 3.4. Element type and implementation

We employ linear elements in this work, specifically using an 8-node hexahedral element (C3D8) for the displacement, magnetic potential, and pressure fields. The choice of C3D8 is based on its ability to capture the necessary physical phenomena with a reasonable computational cost, while maintaining a sufficient level of accuracy in modeling both mechanical and electromagnetic fields. This mixed element should satisfy the LBB (Ladyzhenskaya–Babuska–Brezzi) condition in obtaining accurate and stable solutions (Brezzi and Bathe, 1990; Brezzi and Fortin, 2012; Nemer et al., 2021). To achieve this, the Gauss quadrature degree for the pressure field is set one degree lower than for the displacement and magnetic potential fields. The combination of elements for displacement, potential, and pressure is thus denoted as Q1/Q1/Q0.

We implement the proposed finite element formulation for the coupled magneto-mechanical growth problems using the UEL (user-defined element) subroutines in ABAQUS. The UEL allows for greater flexibility in defining element order, basis functions, and material tangent stiffness, making it ideal for modeling complex coupled physical phenomena.

The input files and UEL subroutines used to generate the results presented in this work are available in the GitHub repository, the link to which can be found in the Supplementary material section.

## 4. Verification and convergence test

In this section, we present a series of tests to validate the proposed finite element framework for simulating material behavior influenced by mechanical forces, magnetic fields, and growth effects. In the first example, we consider the uniaxial loading of a tube under an external magnetic field. In the absence of the stimulated magnetic field  $\mathbf{H}_s$ , the presented model in Section 2 reduces to Zhao's model (Zhao et al., 2019), for which an analytical solution is derived. To evaluate the effect of the stimulated magnetic field on the deformation of the tube, we conduct three cases of simulations: (1) without  $\mathbf{H}_s$  and free space; (2) without  $\mathbf{H}_s$  but with free space; and (3) with  $\mathbf{H}_s$  and free space. In the second example, we consider the compression of a block to check the convergence performance of the proposed finite element framework.

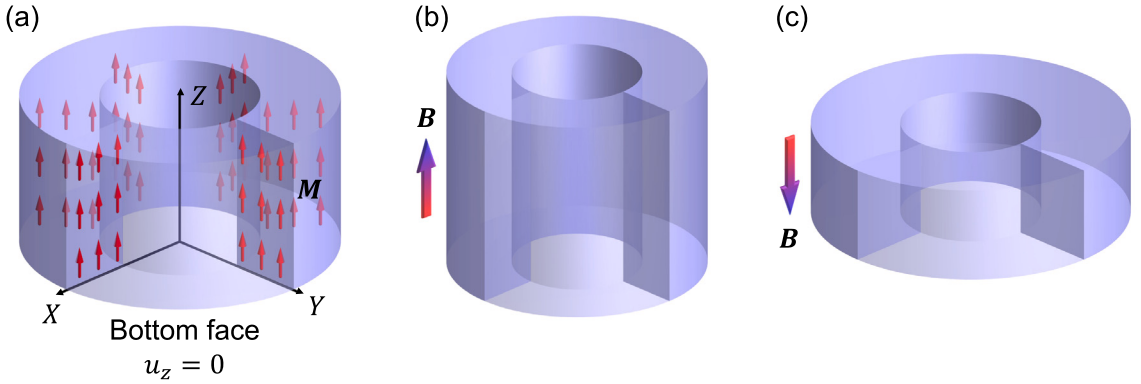


**Fig. 3.** Deformation of a hard magnetic tube under an external magnetic field: (a) reference configuration of the tube with  $\mathbf{M}$  along the  $Z$ -axis; (b) elongation due to external  $\mathbf{B}_a$  along the  $Z$ -axis; (c) shortening under external  $\mathbf{B}_a$  oriented in the negative  $Z$ -direction.

#### 4.1. Uniaxial loading of a tube

As shown in Fig. 3, we consider the axisymmetric deformation of a circular tube, which has a reference configuration  $\mathcal{K}_r = R \times \Theta \times Z = [R_i, R_o] \times [0, 2\pi] \times [0, L]$ . Here,  $L$  denotes the length of the tube,  $R_i$  the inner radius, and  $R_o$  the outer radius. Both the magnetization density  $\mathbf{M} = M_3 \mathbf{e}_3$ , and the external magnetic flux density  $\mathbf{B}_a = B_3 \mathbf{e}_3$  are constant and aligned along the  $Z$ -axis. For simplicity, we assume the tube experiences isotropic growth, yielding a diagonal growth tensor  $\mathbb{G} = g \mathbb{I}$ , where  $g$  is the growth factor. To generate a homogeneous uniaxial deformation along the  $Z$ -axis, the surface at  $Z = 0$  is constrained in the  $Z$ -direction. In addition, the tube is free from both body forces and surface reactions.

In the absence of the stimulated magnetic field  $\mathbf{H}_s$ , our presented model reduces to Zhao's model, and the analytical solution can be derived below. With the current position vector defined as  $\mathbf{x} = r\mathbf{e}_r + Zl/L\mathbf{e}_3$ , the total deformation gradient tensor and the elastic deformation gradient tensor are given by

$$\mathbb{F} = \text{diag} \left( \frac{\partial r}{\partial R}, \frac{r}{R}, \frac{l}{L} \right), \quad \mathbb{A} = g^{-1} \text{diag} \left( \frac{\partial r}{\partial R}, \frac{r}{R}, \frac{l}{L} \right). \quad (54)$$

Considering the incompressibility condition for the elastic deformation gradient tensor,  $J_A = 1$ , from Eq. (10), these expressions simplify to

$$\mathbb{F} = \text{diag} \left( g^3 \frac{LR}{lr}, \frac{r}{R}, \frac{l}{L} \right), \quad \mathbb{A} = \text{diag} \left( g^2 \frac{LR}{lr}, \frac{r}{gR}, \frac{l}{gL} \right). \quad (55)$$

For quantitative analysis, we employ a truly incompressible neo-Hookean constitutive model, where the elastic strain energy function is defined as

$$\Psi_{e,\text{dev}} = J_G \frac{G}{2} (I_{\bar{\mathbb{C}}} - 3), \quad (56)$$

where  $G$  is the shear modulus, and  $I_{\bar{\mathbb{C}}}$  denotes the first invariant of the elastic right Cauchy–Green tensor  $\bar{\mathbb{C}}$ . Subsequently, the effective Cauchy stress is derived as follows:

$$\hat{\sigma} = G J_A^{-5/3} \left( \mathbb{A} \mathbb{A}^T - \frac{1}{3} J_A^{2/3} I_{\bar{\mathbb{C}}} \mathbb{I} \right) - J_G^{-1} \mathbb{F} \mathbf{M} \otimes \mathbf{B}_a + p. \quad (57)$$

By substituting  $J_A = 1$ , the non-zero components of  $\hat{\sigma}$  simplify to

$$\begin{cases} \hat{\sigma}_{rr} = G \left( \frac{g^4 L^2 R^2}{l^2 r^2} - \frac{1}{3} I_{\bar{\mathbb{C}}} \right) + p, \\ \hat{\sigma}_{\theta\theta} = G \left( \frac{r^2}{g^2 R^2} - \frac{1}{3} I_{\bar{\mathbb{C}}} \right) + p, \\ \hat{\sigma}_{zz} = G \left( \frac{l^2}{g^2 L^2} - \frac{1}{3} I_{\bar{\mathbb{C}}} \right) + p - J_G^{-1} B_3 M_3 \frac{l}{L}. \end{cases} \quad (58)$$

In the absence of external mechanical forces, the mechanical equilibrium requires  $\hat{\sigma}_{11} = \hat{\sigma}_{22} = \hat{\sigma}_{33} = 0$ . From Eqs.(58)<sub>1</sub> and (58)<sub>2</sub>, the hydrostatic pressure and circumferential strain  $r/R$  can be derived as

$$p = -3g \frac{L}{l}, \quad \frac{r}{R} = g^{3/2} \sqrt{\frac{L}{l}}. \quad (59)$$

By substituting Eq. (59) into (58)<sub>3</sub>, we obtain the nonlinear relationship between the external magnetic field, growth factor, and the resulting elongation (or shortening) of the tube as

$$\frac{l^3}{L^3} - \frac{B_3 M_3}{g G} \frac{l^2}{L^2} = g^3. \quad (60)$$

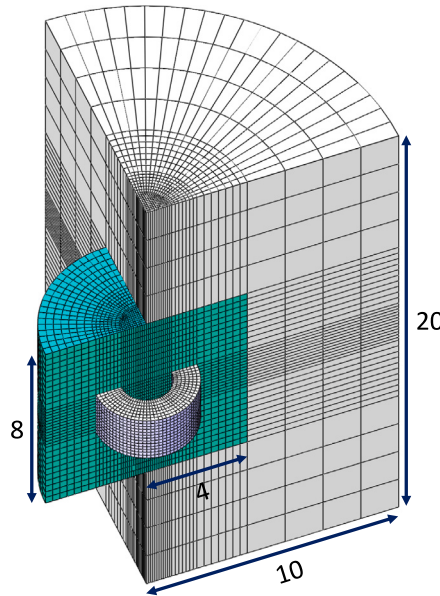


**Fig. 4.** Mesh of the tube and free space.

To evaluate the effect of the stimulated magnetic field on the deformation of the tube, we conduct three cases of simulations:

**Case (1):** without  $\mathbf{H}_s$  and free space.

To facilitate comparison and ensure generality, the system is non-dimensionalized using the following characteristic scales. In the numerical simulation, the geometry of the reference configuration is set as  $L : R_i : R_o = 2 : 1 : 2$ . The magnitude of the external magnetic field  $B_3$ , shear modulus  $G$ , and magnetization density  $M_3$  are set appropriately so that the dimensionless magnetic flux density  $B_3 M_3 / G$  ranges from  $-1$  to  $1$ . The growth factor is set as  $g = \{0.8, 1.0, 1.2\}$  to investigate its effect on the tube's deformability under magnetic stimulation. To enhance computational efficiency, only a quarter of the tubular geometry is modeled. This reduced model is discretized into 1911 8-node hexahedral elements, balancing computational cost with accuracy. Symmetric boundary conditions for displacement are prescribed on the cross-sections. During the loading process, the tube deforms as the growth factor  $g$  varies from 1 to its target value. Subsequently, the external magnetic field is applied while maintaining the growth factor  $g$  at its target value.

**Case (2):** without  $\mathbf{H}_s$  but with free space.

For a magnetized body in free space, the free space domain should be sufficiently large to capture relevant effects. As shown in Fig. 4, we choose a free space domain five times larger than the tube's characteristic dimensions. To avoid abrupt transitions in element size, a transition region of twice the tube size is introduced between the tube and the free space. The tube is discretized into 7644 elements (1911 for a quarter) as in Case (1), and the free space into 75832 elements. To minimize any artificial mechanical influence, the free space is modeled as a soft elastic medium with shear modulus  $G_a \ll G$  (e.g.,  $G_a \approx 10^{-15} G$ ). A nonlocal multi-point constraint (MPC) method further reduces the stiffness of the free space and ensures that the magnetic boundary conditions mimic an infinite external domain. In the  $Z$ -direction, we set  $L_a = 20$ , matching the overall free space scale. For  $X$  and  $Y$  directions inside the tube, we employ  $L_a = 2$ , consistent with the smaller inner free space region. It is anticipated that the MPC method will effectively eliminate the mechanical stiffness of the free space, ensuring that the tube's response remains consistent with the results obtained in Case (1).

**Case (3):** with  $\mathbf{H}_s$  and free space.

In this case, although we keep the dimensionless ratio  $B_3 M_3 G^{-1}$  in the same range as before, the stimulated mechanical and magnetic response may still vary with different choices of  $G$  and  $M_3$ . To ensure realistic parameter magnitudes, we fix the magnetization density at  $M_3 = 120$  kA/m and let  $G = \{60, 120, 240\}$  kPa. The external field  $B_3$  is then adjusted so that  $B_3 M_3 G^{-1}$  remains between  $-1$  and  $1$ . All other finite element settings follow Case (2). While it is feasible to use strictly SI units for magneto-growth problems, the large disparity between mechanical and magnetic parameter magnitudes can lead to ill-conditioned numerical systems. In particular, the stiffness matrix may exhibit entries differing by many orders of magnitude, making convergence under the Newton-Raphson scheme more challenging. To mitigate these issues, we adopt a scaled unit system. Specifically, we measure the applied magnetic flux density  $\mathbf{B}_a$  in mT, and the fields  $\mathbf{H}_a$  and  $\mathbf{H}_s$  in kA/m. Correspondingly, the magnetic permeability of free space is taken as  $0.4\pi N \cdot (kA)^{-2}$ . This approach keeps the mechanical and magnetic variables in comparable ranges and promotes robust convergence.

The relationship between the uniaxial stretch  $l/L$  and the dimensionless magnetic flux density  $B_3 M_3 / G$  is illustrated in Fig. 5(a)-(c). As illustrated in Figs. 5 (a) and (b), the results obtained from the (case of in the absence of  $\mathbf{H}_s$ ) closely align with the analytical

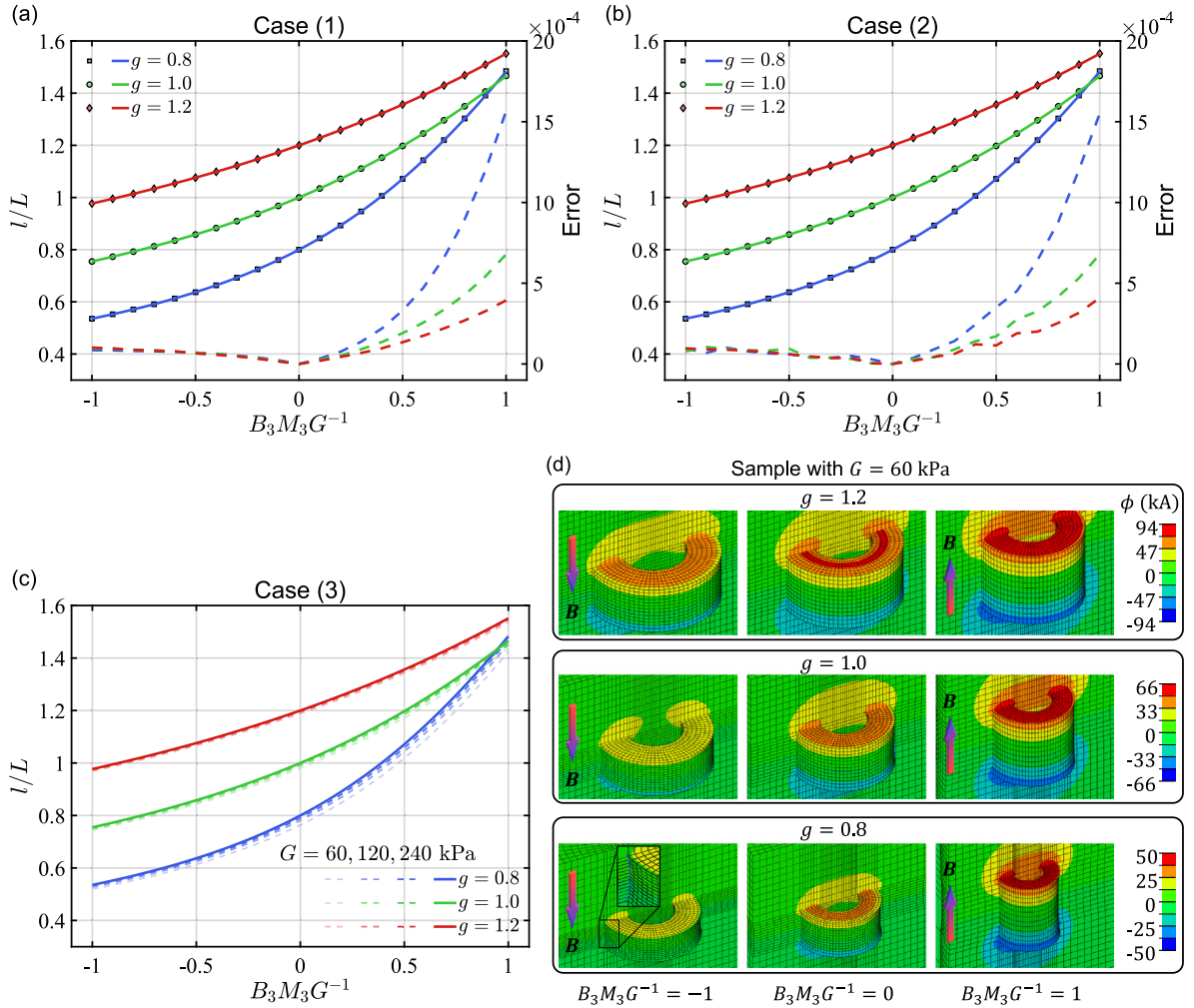


**Fig. 5.** Comparison of analytical (solid lines) and numerical results (scatter points) of the uniaxial stretch  $l/L$  versus dimensionless magnetic flux density  $B_3 M_3 G^{-1}$  for  $g = \{0.8, 1.0, 1.2\}$ : (a) Case 1; (b) Case 2; (c) Case 3. (d) Magnetic potential distribution for Case 3 with  $G = 60$  kPa.

solution. The error between the analytical and numerical results is also represented by the dashed lines in the figures, they show similar trends for different growth factors  $g$ . This result shows that the surrounding mesh has a negligible effect on the tube's deformation. Because the stiffness of the mesh in the free space is effectively eliminated by the nonlocal MPC method. In Case (3) (Fig. 5(c)),  $\mathbf{H}_s$  is taken into account. The solid lines still represent the analytical solution (without  $\mathbf{H}_s$ ), whereas the dashed lines correspond to numerical solutions at different shear moduli  $G = \{60, 120, 240\}$  kPa. When  $G = 240$  kPa (darker dashed lines), the ratio  $G/M_3$  is closer to that in Zhao et al. (2019), and the deviations from the analytical curve are modest. However, for softer materials (e.g.,  $G = 60$  kPa),  $\mathbf{H}_s$  influences the overall deformation due to the lower elastic resistance. In other words, softer structures are more sensitive to additional magnetic fields generated by the magnetized body itself. The results also indicate that the effect of  $\mathbf{H}_s$  can be reasonably neglected for relatively stiff soft materials. In scenarios where the distribution of  $\mathbf{H}_s$  is not of primary interest, a simplified model can be employed to significantly reduce computational cost while maintaining sufficient accuracy.

Fig. 5(d) shows the magnetic potential distribution in the free space for  $G = 60$  kPa. Notably, for certain combinations of growth factor and magnetic flux density, the outer tube boundary undergoes inward concavity, particularly when  $B_3 M_3 G^{-1} = -1$  and  $g = 0.8$ . Such feature cannot be captured by models that ignore  $\mathbf{H}_s$ . Similar effects have also been observed experimentally (see, e.g., Moreno-Mateos et al., 2023). This behavior arises because the local distribution of  $\mathbf{H}_s$  near the edges becomes non-uniform, leading to heterogeneous stresses and an outward pull on the tube boundaries. In fact, residual magnetization in hard-magnetic elastomers can cause spatial variations in the magnetic field, promoting a non-uniform deformation mode, especially in very soft samples.

Overall, for a given increment of magnetic flux density  $\Delta B_3 M_3 G^{-1}$ , the stretch increment  $\Delta l/L$  is inversely related to the growth factor  $g$ . At the same level of magnetic flux density, the tube with a smaller  $g$  is easier to stretch or compress than that with a higher  $g$ . In fact, the tube shrinks when  $g < 1$ , which leads to the condensation of the magnetization density  $\mathbf{M}$ . Consequently, tubes with

smaller  $g$  experience greater extension or compression under the same  $B_3 M_3 G^{-1}$  level, demonstrating that the interplay between growth, magnetization, and material stiffness significantly affects the overall deformation response.

#### 4.2. Mesh convergence study

In this section, we investigate the mesh convergence of the proposed mixed finite element framework applied to hard magnetic hyperelastic materials that incorporate growth effects. To evaluate the robustness and accuracy of our numerical formulation, we utilize the benchmark example introduced by Reese et al. (1999). This benchmark considers a 3D block under large compressive deformations, providing a test for the performance of the numerical framework when handling significant nonlinearities and complex deformation behaviors in such materials. As shown in Fig. 6(a), we investigate the compression of a 3D block with a reference configuration  $\mathcal{K}_r = X \times Y \times Z = [0, 1] \times [0, 1] \times [0, 1]$ . The magnetization density  $\mathbf{M} = M_3 \mathbf{e}_3$  aligns with the  $Z$ -axis, while the external magnetic flux density  $\mathbf{B}_a = B_3 \mathbf{e}_3$  ( $B_3 < 0$ ) is directed along the negative  $Z$ -axis. For simplicity, we assume that the block experiences isotropic growth, yielding a diagonal growth tensor  $\mathbb{G} = 1.05 \mathbb{I}$ . The growth functions in the growth tensors are incorporated as state variables in the subroutine, changing from 1 to the target values during the growth process. This linear evolution can generate excessive residual stresses, leading to instability phenomena. Our previous study (Li et al., 2023b) demonstrated that different growth paths affect the distribution of residual stresses, which may drive the sample into alternative stable morphologies when these stresses are sufficiently large. Unless specified, the loading path of growth function in our simulation is linear by default. Symmetric displacement boundary conditions are prescribed on the surfaces  $X = 0$ ,  $Y = 0$ , and  $Z = 0$ , while the top face has constraints  $u_x = u_y = 0$ . To generate significant compression at the point  $(0, 0, 1)$ , only a quarter of the block  $[0, 0.5] \times [0, 0.5] \times [0, 1]$  is magnetized. For this benchmark problem, the material model is chosen as an incompressible neo-Hookean model with a shear modulus of  $G = 50$  kPa. The magnetization density is set to  $M_3 = 100$  kA/m.

We investigate mesh convergence under two scenarios: with and without free space. In the first scenario, the free space surrounding the block is set to be five times larger than the block's dimensions. To evaluate the solution's accuracy and stability, we incrementally refine the mesh. Each edge of the block is subdivided into {2, 4, 8, 12} elements, resulting in hexahedral meshes with {8, 64, 512, 1728} elements, respectively. For the scenario with free space, the total number of mesh elements increases to {216, 1728, 13824, 21952} due to the additional free space region. The block is compressed by the external  $\mathbf{B}_a$ , where the maximum comparison ratios at point  $(0, 0, 1)$  in different loading cases are shown in Figs. 6 (c) and (d). The reference solutions, depicted by dashed lines, are generated using a model meshed with 4096 elements. Fig. 6(b) presents pressure contour plots for various mesh sizes at  $B_3 M_3 G^{-1} = -3$ . As the mesh refines (from left to right in the figure), the pressure distribution becomes increasingly defined and localized around the magnetized region.

This mesh convergence study demonstrates that the proposed mixed finite element framework achieves numerical stability and accuracy with mesh refinement. The convergence behavior shown in Fig. 6 validates the framework's effectiveness in capturing the complex interactions between magneto-mechanical forces and growth-induced deformations. The results indicate that with sufficient refinement, the solution converges toward the reference solutions, confirming that the framework is both robust and computationally efficient for practical engineering applications. For materials with a not too small ratio of modulus to magnetization, regardless of whether free space is considered, the simulated results remain similar. However, the computational cost is significantly reduced when the free space is not included, showing that the efficiency can be improved by simplifying the model.

## 5. Modulation of surface pattern

In this section, we investigate the tunable surface patterns achieved through the application of an external magnetic field. To generate these surface patterns, growth-induced instability is introduced into the hard-film/soft-substrate structure. We demonstrate that these patterns can be tuned by adjusting the magnetic field.

### 5.1. Experimental setup and results

The preparation of the hard film and soft substrate is illustrated in Fig. 7(a). The materials used are:

- The hard film, made from a mixture of Ecoflex 00-30 Part A, Part B, and NdFeB powder ( $5 \mu\text{m}$ ) in a mass ratio of 1A:1B:1NdFeB. This mixture is stirred uniformly, degassed, injected into a mold, and cured.
- The soft substrate, created from MuMetal-like silicon provided by POSILICON Inc., is prepared with the same process as the hard film.

To achieve specific distributions of the magnetization density  $\mathbf{M}$ , the samples are magnetized in a uniform magnetic field, orienting the magnetic particles. For the first sample, it is folded and placed between the poles of an electromagnet. The second sample is divided into four partitions before magnetization. During the magnetization process, the position and angle of the sample within the magnetic field are controlled to ensure that the internal  $\mathbf{M}$  has the following distributions:

$$\mathbf{M} = \begin{cases} M \mathbf{e}_1, & X \in [0, L/2] \\ -M \mathbf{e}_1, & X \in [L/2, L] \end{cases}, \quad \mathbf{M} = \begin{cases} M(\mathbf{e}_1 + \mathbf{e}_2), & X \times Y \in [L/2, L] \times [L/2, L] \\ M(\mathbf{e}_1 - \mathbf{e}_2), & X \times Y \in [0, L/2] \times [L/2, L] \\ -M(\mathbf{e}_1 + \mathbf{e}_2), & X \times Y \in [0, L/2] \times [0, L/2] \\ M(-\mathbf{e}_1 + \mathbf{e}_2), & X \times Y \in [L/2, L] \times [0, L/2] \end{cases}. \quad (61)$$

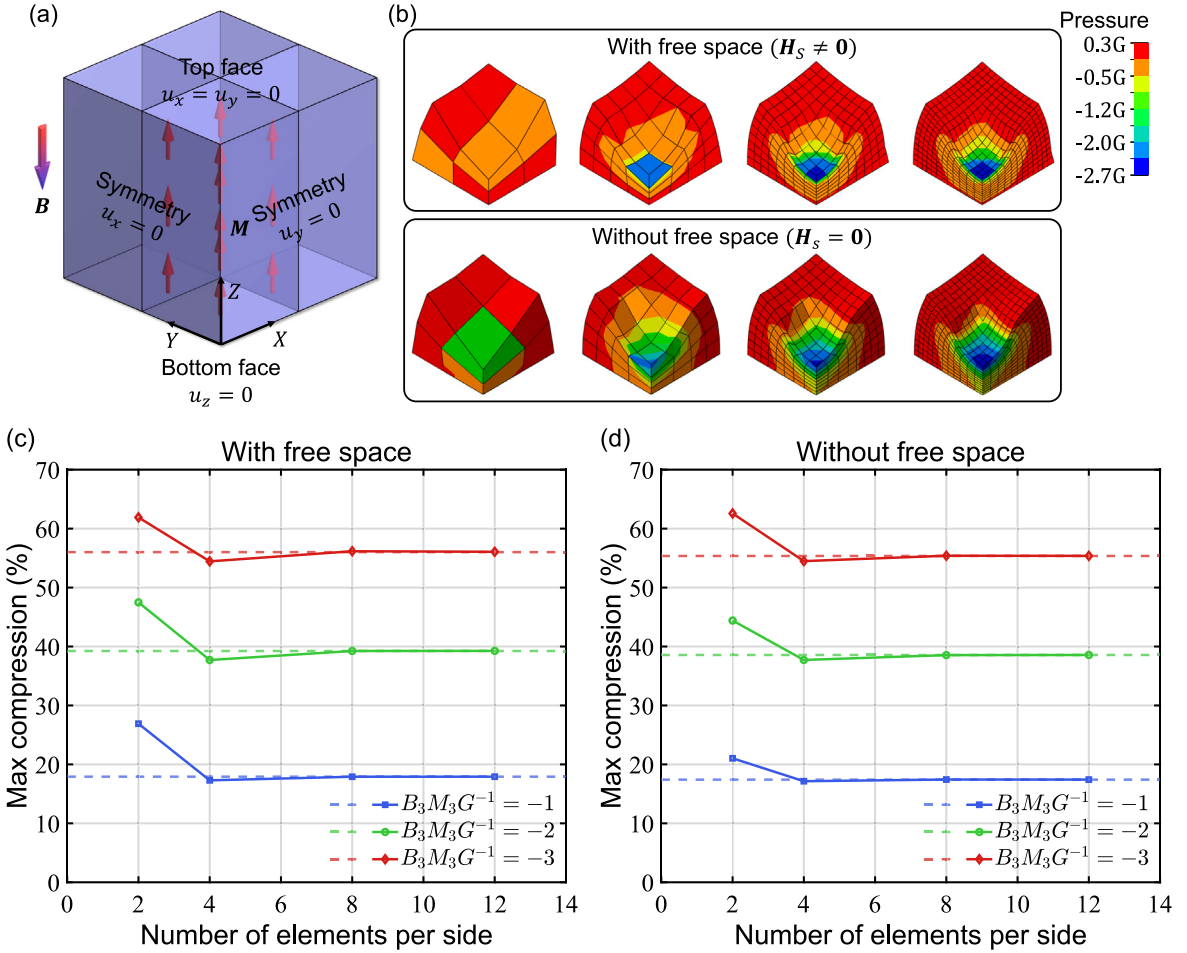


**Fig. 6.** Compression of a block: (a) boundary conditions, the orientation of  $M$  and  $\mathbf{B}_a$ ; (b) contour plots of pressure across different mesh sizes with  $B_3M_3G^{-1} = -3$ . Mesh refinement and the maximum comparison ratios when dimensionless magnetic flux density  $B_3M_3G^{-1} = -\{1, 2, 3\}$  in the scenario of (c) with free space; (d) without free space.

The hard film and the soft substrate are glued together using Ecoflex 00-30 silicone rubber.

As depicted in Fig. 7(b) and (c), the resulting structure has a reference configuration  $\mathcal{K}_r = X \times Y \times Z = [0, L] \times [0, L] \times [0, H_s + H_f]$ , where  $L = 60$  mm,  $H_s = 34.5$  mm, and  $H_f = 3$  mm. We place the samples in a frictionless cubic box so that the sizes of the samples in the  $X$  and  $Y$  directions are constrained when they experience growth and magnetic stimuli. With the applied growth field and external magnetic stimuli, the sample reaches the current configuration  $\mathcal{K}_t = x \times y \times z = [0, L] \times [0, L] \times [0, h]$ .

Symmetric displacement boundary conditions are prescribed on the lateral surfaces  $X = \{0, L\}$ ,  $Y = \{0, L\}$ , and the bottom face  $Z = 0$ . If the external magnetic field is generated by a sufficiently large or uniform magnetic source (such as a solenoid or Helmholtz coil), the applied magnetic field in the sample region can be treated as approximately constant. For simplicity, we assume the external  $\mathbf{B}_a$  is constant and aligned with the  $Z$ -axis. To better understand the magnetic effects on wrinkling, the growth factor  $g$  is applied over the time interval  $t \in [0, 1]$ . From  $t = 1$  to the end of the loading process, the magnitude of  $g$  is held constant. Subsequently, an external magnetic field is introduced, and  $B_3$  is adjusted over the time interval  $t \in [1, 5]$ , as shown in Fig. 7(d). This sequential loading process allows for the examination of the interplay between the growth-induced deformations and the magnetic field on the surface patterns.

For simplicity, we assume that growth occurs in the planar directions ( $X$ - $Y$  plane) of the whole structure, yielding a growth tensor  $\mathbb{G} = \text{diag}(g, g, 1)$ . Generally, the growth effect can be regarded as local volumetric changes. Inspired by the work of Budday et al. (2017), in our experiments, we introduce a pre-strain into the samples to simulate the growth effect. Specifically, we first fabricate the samples to have larger planar dimensions, corresponding to the grown state with stress-free dimensions of  $[0, gL] \times [0, gL]$ . These samples represent the material after growth has occurred. We then squeeze these larger samples into the frictionless cubic box, which has the original, ungrown dimensions of  $[0, L] \times [0, L] \times [0, h]$ . By constraining the samples to these smaller dimensions, we effectively impose a compressive pre-strain that simulates the growth effect. This approach ensures that the growth tensor for the sample inside the box can be considered as  $\mathbb{G} = \text{diag}(g, g, 1)$ . This method allows us to replicate the internal stresses and strains

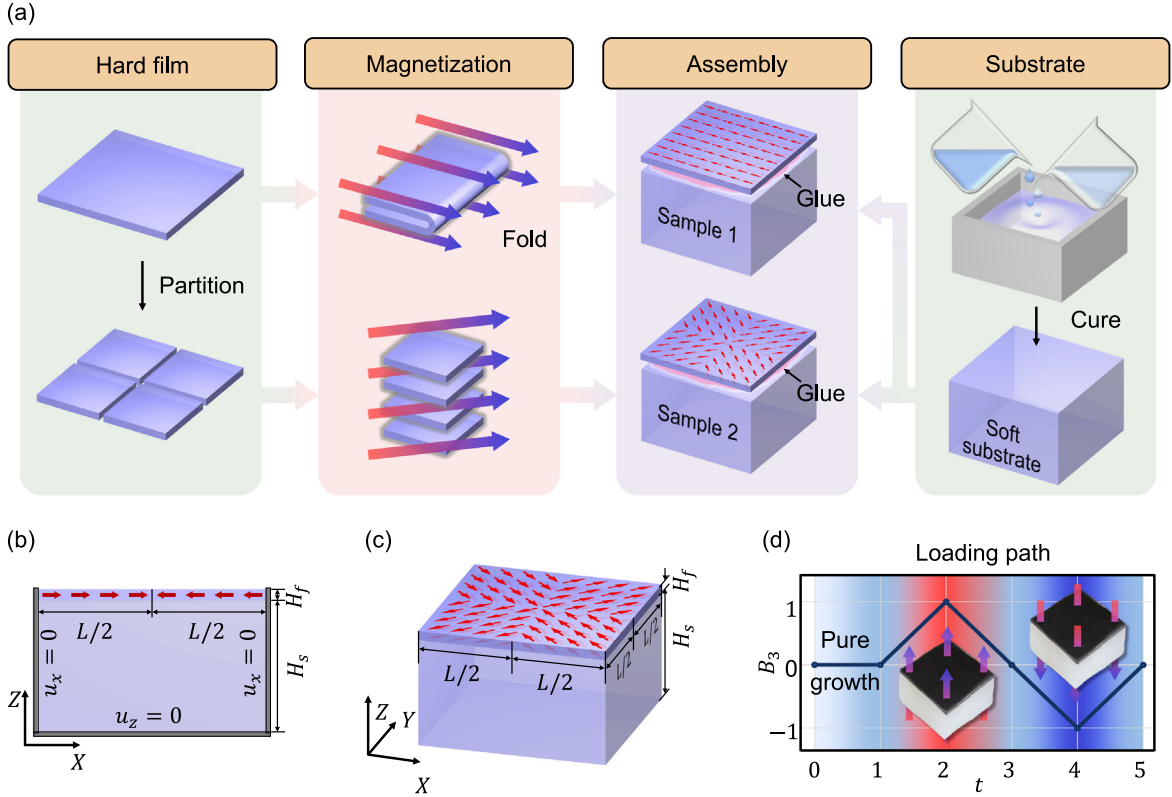


**Fig. 7.** Illustration of the hard film soft substrate samples: (a) Preparation of the samples; (b) geometry of the plane-strain sample; (c) geometry of the wrinkling sample; (d) the loading path.

associated with planar growth, without the need for actual volumetric growth processes within the material. To obtain the shear modulus  $G$  of the film and substrate, uniaxial compression tests are conducted. By adopting the neo-Hookean material model (56), the shear moduli for the film and substrate are calculated from the loading data as  $G_f = 33.9$  kPa and  $G_s = 1.2$  kPa, respectively. Based on a prior work (Wang et al., 2024), the saturated magnetization is estimated as  $M = 44.4$  kA/m.

In our experiments, magnetic loading is applied to modulate the surface patterns. Fig. 8 shows that the sample surface patterns evolve in response to the external magnetic field, with distinct behaviors depending on the direction of  $\mathbf{B}_u$ .

For the sample with a symmetric magnetization (Eq. (61)<sub>1</sub>), we observe from Fig. 8(a) that:

- The grown sample for  $g = 1.1$  is placed in a cubic box, where the inner wall is fully lubricated to reduce friction. At time  $t = 1$ , the sample exhibits instability under axial compression.
- As the magnetic field starts to apply with  $B_3 > 0$ , the surface pattern becomes visibly distorted. At  $t = 2$ , the mode of the surface pattern changes. The wrinkles shift and realign, indicating a transition to a different wrinkling mode.
- Upon unloading at  $t = 3$ , the amplitude of the wrinkles decreases slightly, and the pattern remains convex upward.
- When the magnetic loading is reversed to  $B_3 < 0$ , the center of the sample depresses downward, characterized by the inversion of the previous surface patterns.
- Finally, unloading at  $t = 5$  results in a pattern identical to the one observed at  $t = 1$ .

For the sample ( $g = 1.08$ ) with a quadrantal magnetization distribution (Eq. (61)<sub>2</sub>), as depicted in Fig. 8(b), the response to magnetic loading exhibits similarities to the plane strain case.

These experimental results demonstrate that the surface patterns can be effectively modulated by adjusting the external magnetic field, both in terms of the magnetic loading direction and the distribution of magnetization. The observed wrinkling modes and their transitions under different magnetic loadings provide insight into the tunability of surface patterns in magneto-responsive film–substrate systems.

## 5.2. Numerical simulations

To show the validity and robustness of the proposed numerical scheme, we simulate the evolution of surface patterns under magnetic loading. A nonlinear analysis is used to simulate the post-buckling behavior, where a load perturbation is introduced in

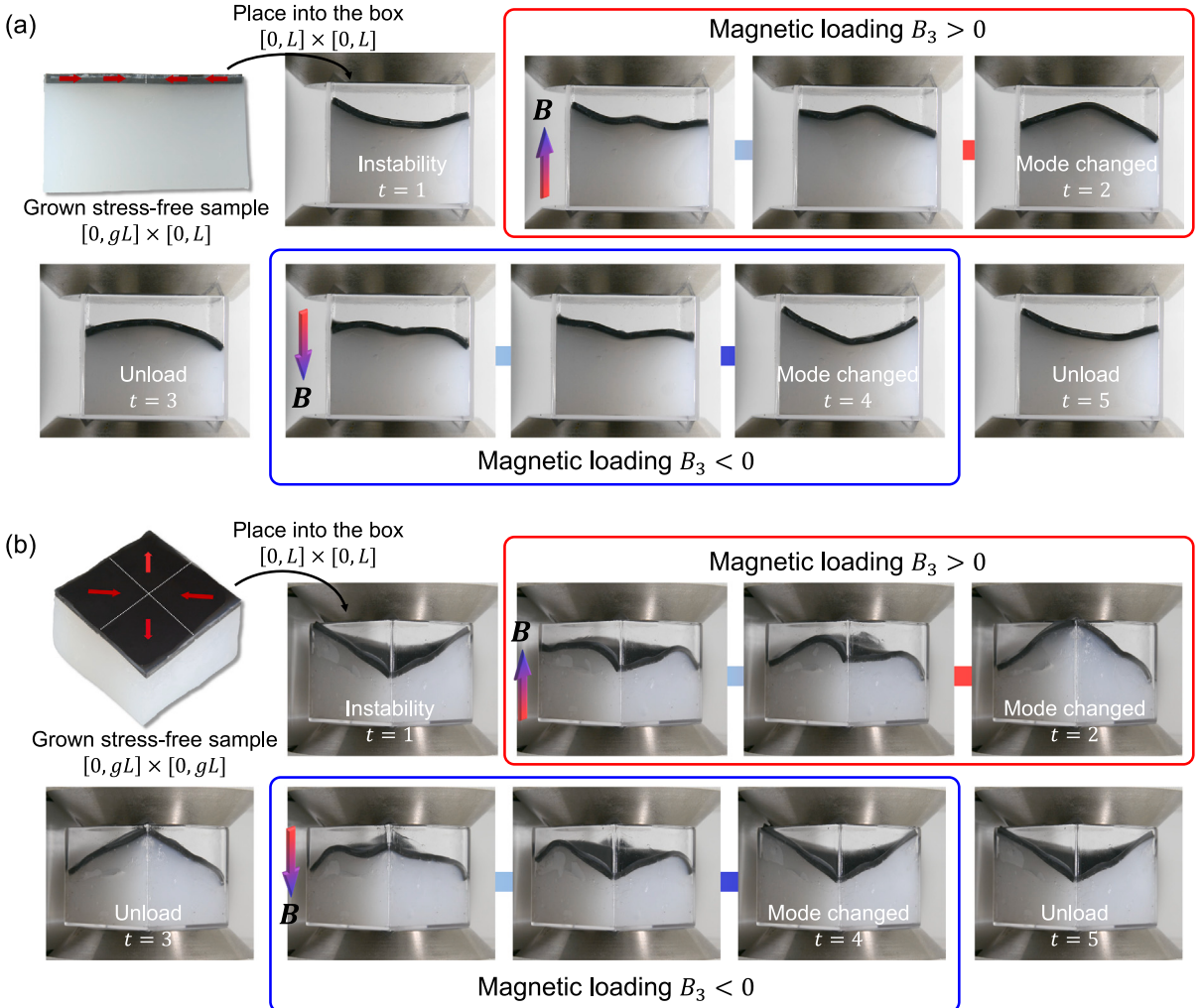


**Fig. 8.** Experimental results showing the evolution of surface patterns under magnetic loading: (a) Sample with symmetric magnetization; (b) Sample with quadrant magnetization.

the growth stage. This perturbation is applied based on the desired shape and is removed at the end of the growth stage. For example, in the first case, we applied traction on the surface of the hard film, with a larger magnitude at the center of the sample and a smaller magnitude at the edges. This load is applied between 0.1 and 0.99 s, and at  $t = 1$  s, the load amplitude is reduced to zero. Compared to the introduction of geometric imperfection, this load perturbation does not affect the subsequent magnetic loading.

In order to save computational costs, we adopt a reduced model that simplifies the finite element model by removing the free space region. Based on the results in Section 4, the shear modulus and magnetization density meet the required conditions, with the stimulated magnetic field  $\mathbf{H}_s$  being negligible. The sample with symmetric magnetization is discretized into 3960 elements, while the sample with quadrant magnetization is discretized into 10368 elements. In Appendix B, we provide the results of the full model with free space for the sample with symmetric magnetization, which show deformation similar to the reduced model.

Fig. 9(a) and (b) show the progressive deformation and stress distributions resulting from applied growth and magnetic influences. As the growth factor increases from 1 to  $g$ , the sample experiences growth-induced instability, leading to surface pattern formation. The magnetic loading process is consistent with the experimental setup described above. The magnitudes for the applied magnetic field are 10 mT and 100 mT for the samples with symmetric and quadrant magnetization, respectively. The simulated evolution processes are in good agreement with the experimental results given in Fig. 8, showing that the proposed numerical scheme is capable of describing such instability phenomena.

To further elucidate the mechanisms of these observed phenomena, the variations in elastic and magnetic potential energy profiles of the samples over time are illustrated in Fig. 9(c) and (d). When an external magnetic flux density  $\mathbf{B}_a$  is applied, the remanent magnetization  $\mathbf{M}$  in the sample tends to align with  $\mathbf{B}_a$ . This alignment reduces the magnetic potential energy  $\Psi_m$ , which

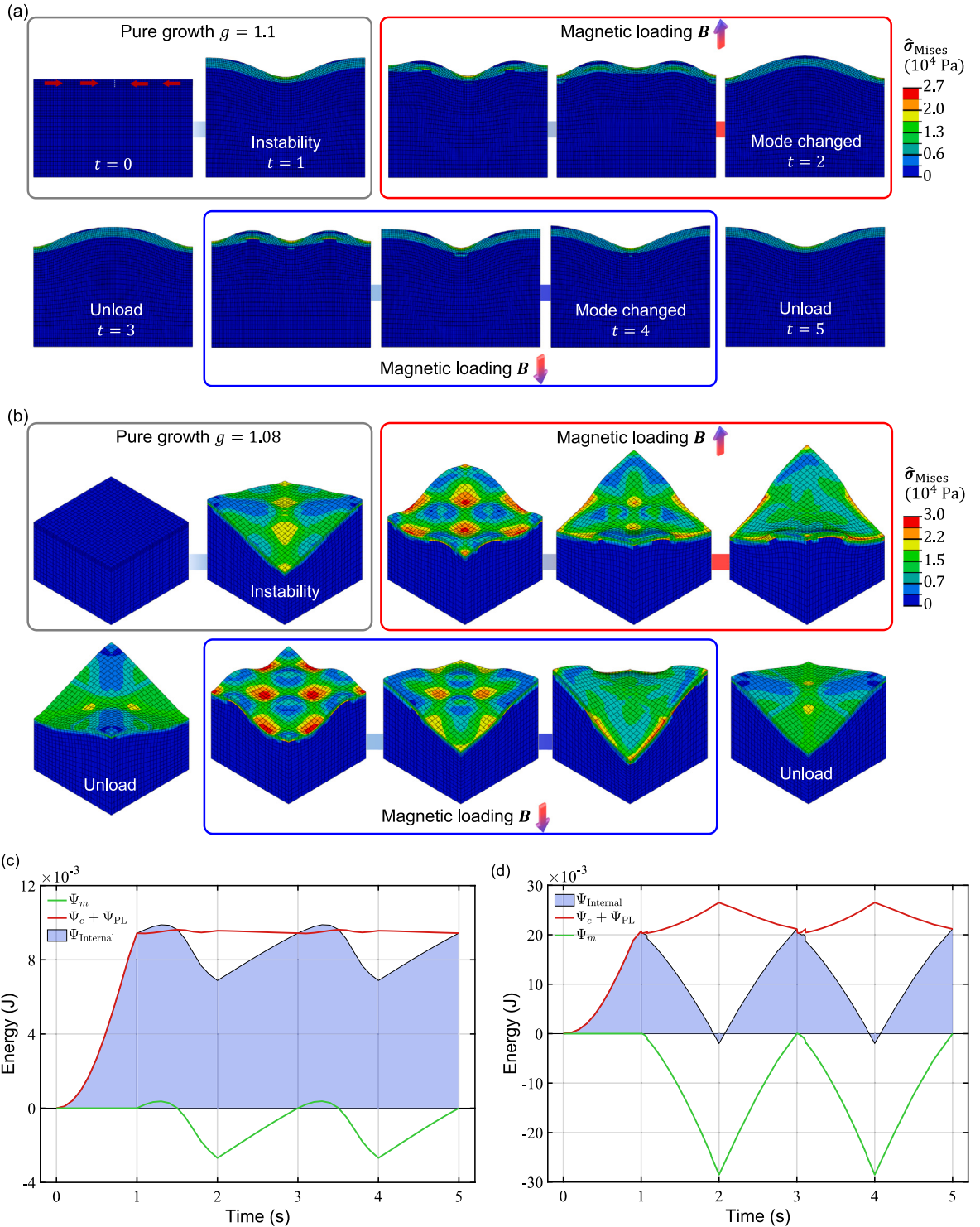


**Fig. 9.** Mises stress contours of the samples over the interval  $t \in [0, 5]$ : (a) symmetric magnetization sample; (b) quadrant sample; (c), (d) the elastic and magnetic potential energy profiles of the two samples over time.

is similar to the gravitational potential energy. To analyze the evolution of the system's energy, we compare the total energy of the samples at  $t = 1$  (before magnetic loading) and  $t = 5$  (after magnetic unloading). Under the condition shown in Fig. 9(c), the total energy of the sample after unloading nearly returns to a level comparable to the initial state. This indicates that the elastic potential

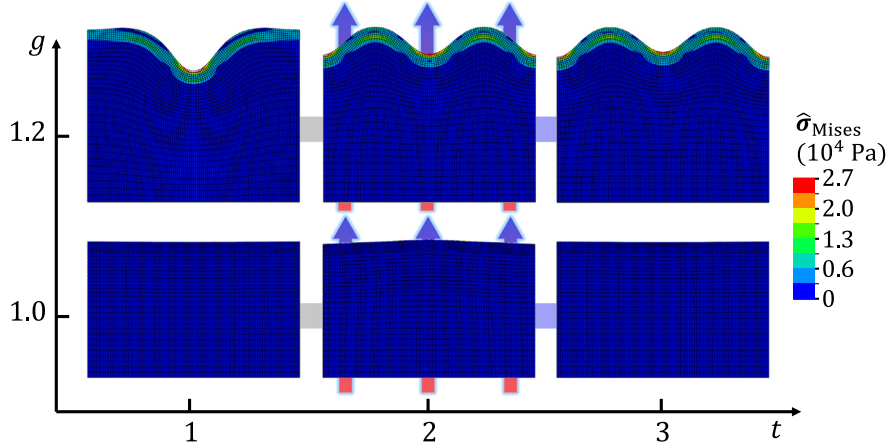


**Fig. 10.** Wrinkling deformation and stress contour of the film–substrate sample under plane strain condition, where the growth factors  $g = \{1.0, 1.2\}$ .

energy stored in the material is fully released upon the removal of the magnetic field, resulting in minimal residual internal stress and bringing the system's energy back close to its initial value. In contrast, under the condition depicted in Fig. 9(d), the total energy after unloading is higher than the initial state, suggesting that some of the elastic potential energy remains unreleased. We hypothesize that this is related to the larger magnetic loading and the resulting instability modes, which lead the system to form a metastable state with slightly higher energy. Corresponding stress distribution in Fig. 9(b) also shows that certain local regions of the sample retain high von-Mises stress after unloading, corroborating the increase in total energy. This indicates that after magnetic loading and unloading cycles, the energy of samples undergoing growth-induced instability may exhibit residuals and fluctuations to some extent, potentially impacting subsequent deformation behavior and performance.

To explore how growth factors influence pattern evolution, we adjust  $g$  in the plane strain example to  $\{1.0, 1.2\}$  (see Fig. 10). In the absence of growth ( $g = 1.0$ ), the sample deforms solely in response to the applied magnetic field, leading to relatively modest wrinkle amplitudes. As  $g$  increases to  $g = 1.2$ , growth-induced residual stresses amplify wrinkling. However, despite the application of the magnetic field, the wrinkle pattern does not undergo any orientation change as previously observed. A higher level of external magnetic field would be required to overcome the elevated elastic energy and modulate the wrinkles.

From the perspective of energy, when  $g = 1$ ,  $\Psi_m$  decreases with increasing  $\mathbf{B}_a$ . This is accompanied by the generation of elastic strain due to magnetic body forces,  $\text{Div}(\mathbf{M})\mathbf{B}_a$  (can be derived from Eq. (34)<sub>1</sub>). When  $g > 1$ , the elastic strain energy rises during the pure growth process, corresponding to the onset of the wrinkle instability. During the application of  $\mathbf{B}_a$  over  $t \in [1, 2]$ , the magnetic potential energy increases first and then drops at the point where the total elastic energy ( $\Psi_e + \Psi_{PL}$ ) reaches a critical level, triggering a wrinkle reorientation. At sufficiently high  $g$  (e.g.,  $g = 1.2$ ), the increased elastic strain dominates the response, preventing significant wrinkle reorientation despite changes in  $\Psi_m$ . Consequently, the accumulated magnetic potential  $\Psi_m$  is no longer strong enough to overcome this larger energy barrier, meaning that further increases in  $\mathbf{B}_a$  are necessary to induce any orientation shift under higher growth conditions.

### 5.3. Discussion

The experimental and numerical investigations in this study demonstrate the potential of external magnetic fields to modulate surface patterns in magneto-active film–substrate systems. By combining growth-induced instability with targeted magnetic loading, tunable surface patterns are achieved. The results indicate that both the direction and magnitude of the magnetic field, along with the specific distribution of magnetization within the sample, are crucial in determining the final wrinkle configuration. The introduction of growth is found to significantly enhance wrinkle amplitude, suggesting that growth-induced residual stresses can effectively compensate for the typically small deformations in magneto-polymers. Additionally, to achieve the transformation of surface patterns, the magnetic potential energy ( $\Psi_m$ ) must be sufficient to overcome the energy barrier imposed by the elastic stability of the sample. The observed multi-stable states and the reversible switching between different wrinkle patterns underscore the potential for designing adaptive surface structures with controllable mechanical and functional properties.

Although there are noticeable discrepancies between the two sets of results, our model captures the primary characteristics of the deformation behavior, indicating its fundamental validity. The consistency of major features between the model and experimental observations suggests that the core mechanisms are represented. Specifically, differences are observed in the amplitude of the wrinkles exhibited by the samples. In both cases, the experimental results exhibit larger wrinkle amplitudes compared to the numerical simulation, particularly under higher magnetic loads. Actually, the existence of instability within our system introduces significant uncertainties, making it challenging to have precise quantitative descriptions. Specifically, the deformation resulting from such instabilities is highly sensitive to material parameters, growth factors, and boundary conditions. This sensitivity complicates the accurate modeling and prediction of deformation modes. The other factors could contribute to these discrepancies: (1) In our

experiments, the samples are relatively large, and the magnetic field generated by the electromagnet may not be perfectly uniform across the entire sample. The non-uniformity of the magnetic field can lead to variations in the magnetic forces acting on different regions of the sample, resulting in complex deformation patterns that are not captured by the numerical simulations, which assume a uniform magnetic field. (2) Although the samples are placed in a frictionless cubic box in both experiments and simulations, achieving perfectly frictionless conditions in practice is challenging. Any residual friction between the sample and the box walls can influence the deformation patterns by constraining the lateral movement of the sample, leading to discrepancies between experimental observations and numerical predictions.

## 6. Modulation of biological morphogenesis

Inspired by the work of [Yu and Chen \(2024\)](#), we apply our numerical framework to explore a biological phenomenon: the *inversion* process of the algal genus Volvox (as shown in [Fig. 11\(a\)](#)). The inversion process in the Volvox embryo is a fascinating and complex biological event ([Cole and Reedy, 2003](#); [Höhn et al., 2015](#); [Haas and Goldstein, 2015](#)). Initially, the flagella (the whip-like structures used for movement) of the cells are oriented inward, facing the inside of the sphere. As the inversion process begins, the Volvox colony starts to roll over itself, initiating a coordinated movement where the outer layer of cells begins to turn inward. As the rolling motion continues, the spherical structure transforms into a deep cup-like shape. After inversion, the cells with flagella are positioned on the outside, allowing the Volvox to swim efficiently. The fully inverted and mature Volvox colony is shown in [Fig. 11\(b\)](#), with the flagella correctly positioned on the outside, enabling motility and proper functioning for further development and reproduction. To demonstrate the capabilities of our proposed numerical framework, we employ a magnetic field as an external and controllable stimulus to simulate the deformation during inversion. While magnetic fields are not a naturally occurring factor in the Volvox inversion process, they serve here as a computational analogy to explore the mechanics of inversion. This approach allows us to investigate how external forces might modulate and drive complex shape transformations, offering insights into general morphogenetic mechanisms. Moreover, the actual biological driving forces of Volvox inversion are known to involve a combination of the relocation of the cytoplasmic bridges, differential cell growth, and tissue elasticity ([Matt and Umen, 2016](#)). The inversion process in Volvox provides inspiration for the design of biomimetic devices, such as self-reconfiguring robots and deployable medical devices.

For the sake of computational efficiency, the simulation is divided into two stages. The first stage involves growth from a circular plate-like structure to an approximately spherical shell. This stage accounts for the biological growth factors that cause the expansion and curvature of the structure, mimicking the natural development of the Volvox embryo. The second stage simulates the inversion process itself, which is driven by an external magnetic field. Here, we conceptualize the artificial Volvox as a soft shell-like structure embedded with responsive magnetic particles. The magnetic actuation triggers the inversion by inducing localized forces that mimic the deformation observed in the biological system.

As depicted in [Fig. 11\(c\)](#), the reference configuration of the sample is a circular plate with inner radius  $r_i = 0.01$ , outer radius  $r_o = 0.5$ , and thickness  $h = 0.04$ . The axis of symmetry of the plate is located at  $X = Y = 0$ . The shear modulus of the plate is set as  $G = 33.3$  kPa. To improve computational efficiency, only a quarter of the plate is modeled, which is meshed into 7840 hexahedral elements. Symmetric boundary conditions of displacement are prescribed on the cross-sections. To fully remove the rigid body motion, the inner edge of the bottom face is constrained in the  $Z$ -direction. As shown in [Fig. 11\(c\)](#), the magnetization density  $\mathbf{M}$  (kA/m) has a non-uniform distribution

$$\mathbf{M} = 10^2 \sqrt{X^2 + Y^2} (X\mathbf{e}_1 + Y\mathbf{e}_2 + \mathbf{e}_3), \quad (62)$$

while the external  $\mathbf{B}_a = B_3\mathbf{e}_3$  is aligned with the  $Z$ -axis.

In the loading process, the plate deforms as the growth tensor gradually transitions from  $\mathbb{I}$  to the target  $\mathbb{G}$  over the time interval  $t \in [0, 1]$ :

$$\begin{aligned} \mathbb{G} &= \text{diag}\{\lambda, \lambda, 2\}, \\ \lambda &= -\frac{2\alpha R(Z-1)}{R^2 + \alpha^2(X^2 + Y^2)}, \quad \alpha = 1.6, \quad R = 0.5. \end{aligned} \quad (63)$$

In the growth process shown in [Fig. 11\(d\)](#), the plate undergoes deformation driven by the prescribed growth tensor  $\mathbb{G}$ . This tensor controls the expansion and shape change of the plate, transitioning it from its initial flat configuration to a more complex three-dimensional structure. Then, the external  $\mathbf{B}_a$  starts to apply to the grown sample while the growth tensor remains at the target  $\mathbb{G}$  in (63). As depicted in [Fig. 11\(e\)](#), this magnetic loading during the time interval  $t \in [1, 2]$  causes the structure to invert, with the initially convex shape transforming into a concave form, mimicking the inversion process observed in biological systems. The magnetic forces drive this inversion by creating localized stresses that cause the structure to fold and flip over. Upon unloading ( $t \in [2, 3]$ ), with  $\mathbf{B}_a$  removed, the structure returns to a sphere-like shell configuration; it still remains in the inverted position, however.

The numerical framework employed in this study simulates the complex deformation processes inspired by Volvox inversion. The two-stage simulation, involving growth-driven deformation followed by magnetic actuation, captures the transition from a flat plate to a spherical structure and its subsequent inversion. The ability to simulate such intricate behaviors demonstrates the robustness and versatility of the numerical approach, which can be applied to the design and optimization of adaptive, shape-morphing materials and devices.

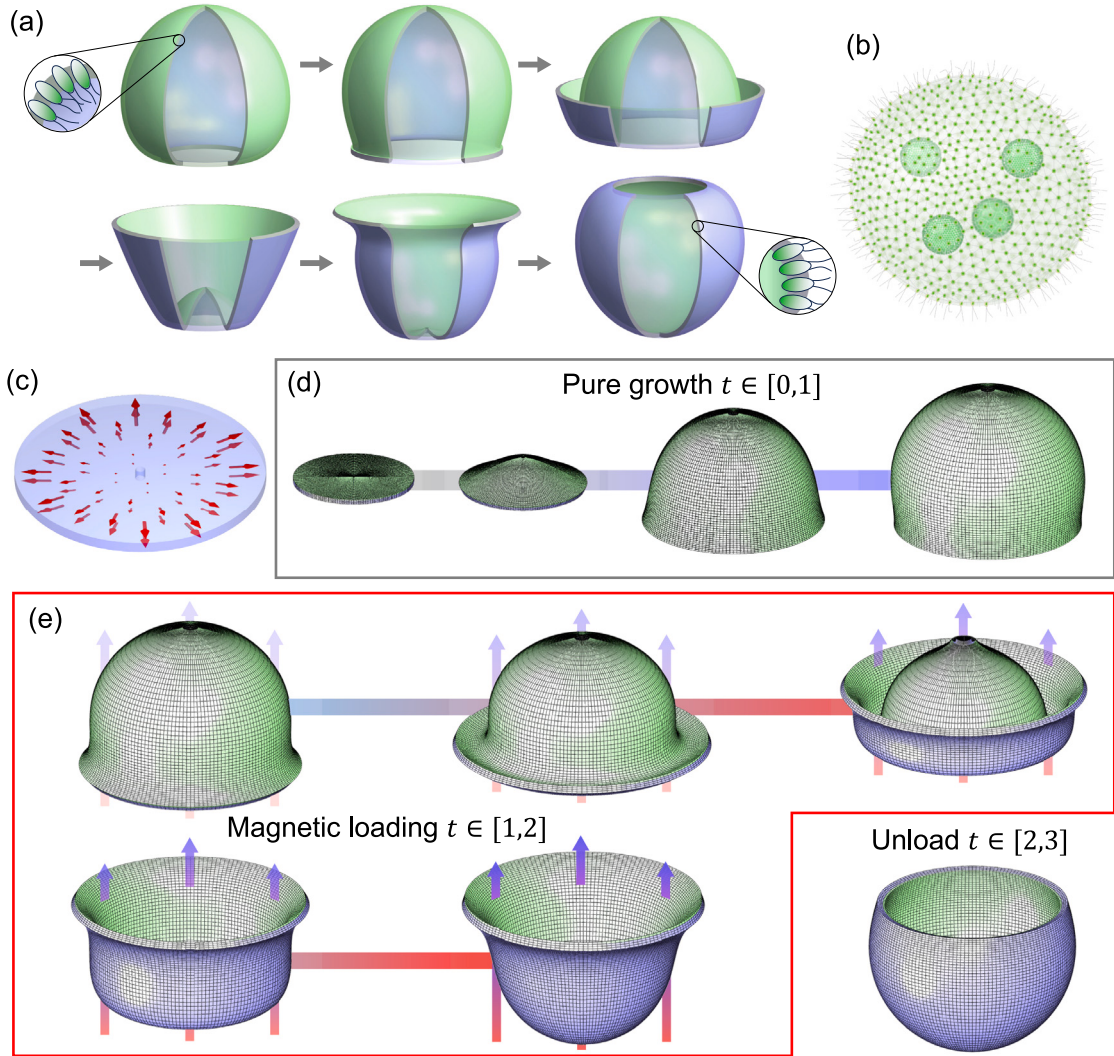


**Fig. 11.** (a) Illustration of the inversion process in a Volvox embryo; (b) Fully inverted and mature Volvox colony with flagella positioned on the outside (image taken from [Wikimedia Commons](#), licensed under CC BY-SA 4.0); (c) Reference configuration of the circular plate; (d) Growth process of the plate; (e) Magnetic loading process.

## 7. Conclusions

This study proposes a numerical framework to understand the coupled magneto-mechanical growth behavior of hyperelastic materials. The main findings are summarized as follows:

- We develop the 3D governing equations and finite element formulations for coupled magneto-mechanical growth in soft materials. This extension provides a theoretical basis for understanding the interplay between magnetic fields, mechanical forces, and growth behavior in soft materials.
- Benchmark tests show agreement with analytical solutions, verifying the framework's robustness and accuracy across various mesh sizes. If the material is relatively stiff and the magnetization is not particularly strong, the reduced model can be used, as it provides a good approximation while significantly reducing computational cost.
- By combining growth-induced instabilities with external magnetic fields, we demonstrate the tunability of surface patterns in magneto-active film–substrate systems. The introduction of growth enhances the responsiveness of these materials, which is also demonstrated experimentally.
- Inspired by the inversion process in Volvox embryos, we simulate similar deformations in magneto-active plates. These simulations show the capability to mimic the complex shape transformations observed in biological systems, suggesting potential applications in designing adaptive, shape-morphing materials and devices.

The proposed framework can be further extended to diverse applications, including soft robotics, flexible electronics, and bio-inspired engineering. It also opens avenues for further exploration into the multi-physical behaviors of soft materials, where growth, magnetic fields, and mechanical forces interact in complex ways.

Despite the proposed framework has demonstrated capabilities in modeling coupled magneto-mechanical growth in soft materials, certain limitations and areas for improvement are identified. Firstly, the computational resource consumption is substantial. The current framework's handling of free space requires significant memory and computation time, as the free space mesh typically constitutes the major part of the model. This approach is neither economical nor practical for engineering applications. Future work may focus on enhancing computational efficiency. Developing adaptive or hybrid algorithms for free space modeling, such as boundary element methods or fluid-inspired methods, could substantially reduce computational consumption. Additionally, extending the framework to incorporate advanced constitutive models (e.g., Ogden or Gent models) would improve its ability to capture nonlinear elastic responses. Integrating viscoelasticity is another critical step to model time-dependent material behavior observed in experimental studies. Finally, extending the theory to account for growth-induced variations in material properties, such as elastic modulus, would further bridge the gap between simulations and real-world material behavior.

#### CRediT authorship contribution statement

**Zhanfeng Li:** Writing – original draft, Validation, Software, Funding acquisition, Formal analysis, Data curation. **Yafei Wang:** Writing – review & editing, Visualization, Software, Methodology, Formal analysis, Conceptualization. **Zuodong Wang:** Methodology, Investigation, Data curation. **Chennakesava Kadapa:** Writing – review & editing, Methodology, Investigation, Formal analysis, Conceptualization. **Mokarram Hossain:** Writing – review & editing, Project administration, Methodology, Investigation, Funding acquisition, Formal analysis, Conceptualization. **Xiaohu Yao:** Project administration, Investigation, Formal analysis. **Jiong Wang:** Writing – review & editing, Project administration, Methodology, Funding acquisition, Formal analysis, Conceptualization.

#### Declaration of competing interest

The authors declare the following financial interests/personal relationships which may be considered as potential competing interests: If there are other authors, they declare that they have no known competing financial interests or personal relationships that could have appeared to influence the work reported in this paper.

#### Acknowledgments

J.W. acknowledges support from the National Natural Science Foundation of China (Project No. : 12172133) and the Natural Science Foundation of Guangdong Province, China (Project No. : 2022A1515010653). M.H. acknowledges the support of the Royal Society (UK) through the International Exchange Grant (IEC/NSFC/211316). Z.L. gratefully acknowledges support from the Postdoctoral Innovation Talent Support Program of China (No.: BX20240119).

#### Appendix A. The second variation of energy functional

The second variation of the total energy functional  $\Pi$  for the magneto body can be written as

$$\begin{aligned}
 d(\delta\Pi) = & \int_{\mathcal{K}_r} d \left[ \text{tr}(\delta \mathbb{F} \mathbb{S}) + \delta p \left( J - J_G - \frac{p}{\kappa} J_G \right) + p \delta J \right. \\
 & + \mu_0 J (\mathbb{F}^{-T} (\delta \mathbb{F}^T) \mathbf{H}_s + \text{grad} \delta \phi) \cdot \mathbf{m} - \mu_0 (\mathbf{H}_a + \mathbf{H}_s) \cdot \delta \mathbb{F} \mathbf{M} \\
 & \left. - \frac{1}{2} \mu_0 (\delta J) \mathbf{H}_s \cdot \mathbf{H}_s + \mu_0 J \mathbf{H}_s \cdot (\mathbb{F}^{-T} (\delta \mathbb{F}^T) \mathbf{H}_s + \text{grad} \delta \phi) \right] dV \\
 = & \int_{\mathcal{K}_r} \left\{ \delta u_{i,j} \left[ F_{jI} \frac{\partial \bar{S}_{ji}}{\partial F_{kl}} F_{lI} + p J (\delta_{ij} \delta_{kl} - \delta_{jk} \delta_{il}) \right] du_{k,l} \right. \\
 & + \delta u_{i,j} \mu_0 J (\phi_{,i} \delta_{kj} + \phi_{,j} \delta_{ik} - \phi_{,k} \delta_{ij}) d\phi_{,k} \\
 & + \delta \phi_{,i} \mu_0 J (\phi_{,i} \delta_{kj} + \phi_{,j} \delta_{ik} - \phi_{,k} \delta_{ij}) du_{j,k} - \delta \phi_{,i} \mu_0 J \delta_{ij} d\phi_{,j} \\
 & \left. + J \delta p du_{i,i} - \delta p \frac{J_G}{\kappa} dp + J \delta u_{k,k} dp \right\} dV \\
 = & \int_{\mathcal{K}_r} (\delta u_{i,j} \mathbb{P}_{ijkl} du_{k,l} + \delta u_{i,j} \mathbb{P}_{ijk} d\phi_{,k} + \delta \phi_{,i} \hat{\mathbb{P}}_{ijk} du_{j,k} + \delta \phi_{,i} d_{ij} d\phi_{,j}) dV \\
 & + \int_{\mathcal{K}_r} \left( \delta p du_{i,i} + \delta u_{k,k} dp - \delta p \frac{J_G}{\kappa J} dp \right) dV,
 \end{aligned} \tag{A.1}$$

where the relations below are used

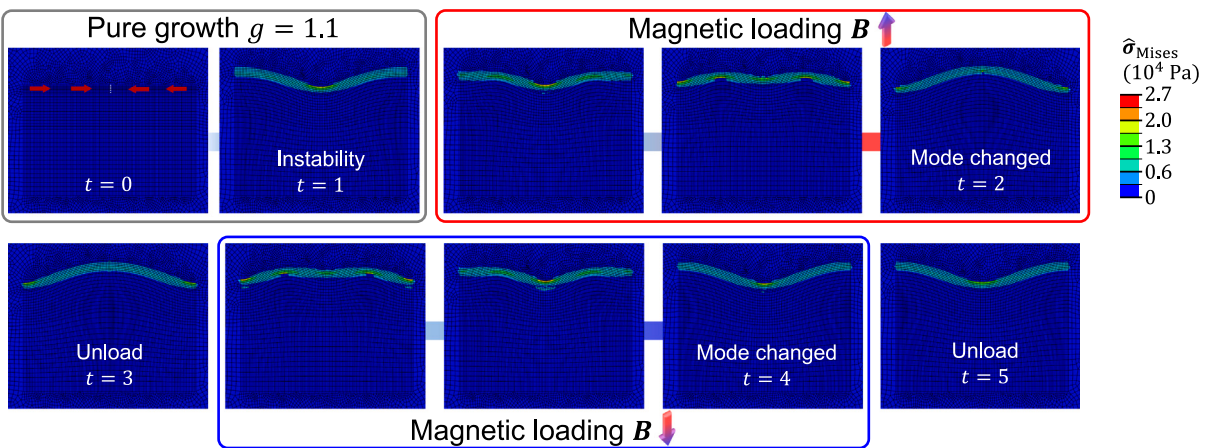


**Fig. B.12.** Mises stress contours of the sample over the interval  $t \in [0, 5]$ .

$$\begin{aligned} d(\delta J) &= \delta u_{i,j} J (\delta_{ij} \delta_{kl} - \delta_{jk} \delta_{il}) du_{k,l}, \\ \bar{S}_{Ji} &= \frac{\partial \Psi_e}{\partial F_{IJ}} + \frac{\partial \Psi_m}{\partial F_{IJ}} = \frac{\partial \Psi_e}{\partial A_{IM}} G_{JM}^{-1} + \frac{\partial \Psi_m}{\partial F_{IJ}}, \\ \mathbb{S}_{ijkl} &= J^{-1} F_{jJ} \frac{\partial \bar{S}_{Ji}}{\partial F_{kl}} F_{lL} + p (\delta_{ij} \delta_{kl} - \delta_{jk} \delta_{il}), \\ \mathbb{P}_{ijk} &= \hat{\mathbb{P}}_{ijk} = \mu_0 (\phi_i \delta_{kj} + \phi_j \delta_{ik} - \phi_k \delta_{ij}), \\ d_{ij} &= -\mu_0 \delta_{ij}. \end{aligned}$$

For the free space, the second variation of the energy functional can be obtained by simply setting magnetization  $\mathbf{M} = \mathbf{0}$  in the above equation.

## Appendix B. The simulated results of the full model

In this finite element model, the free space region is included. The sample is discretized into 3960 elements, while the free space region (5 times large as the sample) is meshed with 6706 elements. The simulated results of the full model, shown in Fig. B.12, are similar to those obtained from the reduced model. However, the computational cost of the full model is significantly higher. By comparing the results of the full and reduced models, we find that the free space region has a negligible effect on the deformation of the sample. Therefore, if the effect of the stimulated magnetic field  $\mathbf{H}_s$  is not a primary concern, the reduced model is recommended for efficiency.

## Appendix C. Supplementary data

Video S1: The experimental and simulated deforming processes of the film-substrate and the Volvox embryo examples.  
 .INP and .FOR files: the ABAQUS input files for the examples and the related UEL subroutine files. All the codes are available at <https://github.com/Jeff97/Magneto-growth-MixedFEM>

Supplementary material related to this article can be found online at <https://doi.org/10.1016/j.jmps.2025.106089>.

## Data availability

Data will be made available on request.

## References

- Abdel Fattah, A.R., Kolaitis, N., Van Daele, K., Daza, B., Rustandi, A.G., Ranga, A., 2023. Targeted mechanical stimulation via magnetic nanoparticles guides in vitro tissue development. *Nat. Commun.* 14 (1), 5281.
- Ambrosi, D., Ateshian, G.A., Arruda, E.M., Cowin, S.C., Dumais, J., Goriely, A., Holzapfel, G.A., Humphrey, J.D., Kemkemer, R., Kuhl, E., 2011. Perspectives on biological growth and remodeling. *J. Mech. Phys. Solids* 59 (4), 863–883.
- Ambrosi, D., Ben Amar, M., Cyron, C.J., DeSimone, A., Goriely, A., Humphrey, J.D., Kuhl, E., 2019. Growth and remodelling of living tissues: Perspectives, challenges and opportunities. *J. R. Soc. Interface* 16 (157), 20190233.
- Armstrong, J.P.K., Stevens, M.M., 2020. Using remote fields for complex tissue engineering. *Trends Biotechnol.* 38 (3), 254–263.
- Ben Amar, M., Goriely, A., 2005. Growth and instability in elastic tissues. *J. Mech. Phys. Solids* 53 (10), 2284–2319.

- Bonet, J., Wood, R.D., 2008. Nonlinear Continuum Mechanics for Finite Element Analysis, second ed. Cambridge University Press.
- Brezzi, F., Bathe, K.J., 1990. A discourse on the stability conditions for mixed finite element formulations. *Comput. Methods Appl. Mech. Engrg.* 82 (1), 27–57.
- Brezzi, F., Fortin, M., 2012. Mixed and Hybrid Finite Element Methods, vol. 15, Springer Science & Business Media.
- Brown, W.F., 1966. Magnetoelastic Interactions. Springer.
- Budday, S., Andres, S., Walter, B., Steinmann, P., Kuhl, E., 2017. Wrinkling instabilities in soft bilayered systems. *Philos. Trans. Ser. A, Math. Phys. Eng. Sci.* 375 (2093), 20160163.
- Bustamante, R., Dorfmann, A., Ogden, R.W., 2008. On variational formulations in nonlinear magnetoelastostatics. *Math. Mech. Solids* 13 (8), 725–745.
- Chester, S.A., Di Leo, C.V., Anand, L., 2015. A finite element implementation of a coupled diffusion-deformation theory for elastomeric gels. *Int. J. Solids Struct.* 52, 1–18.
- Chokalingam, S., Cohen, T., 2024. A large deformation theory for coupled swelling and growth with application to growing tumors and bacterial biofilms. *J. Mech. Phys. Solids* 187, 105627.
- Cleary, J.M., Hancock, W.O., 2021. Molecular mechanisms underlying microtubule growth dynamics. *Curr. Biol.* 31 (10), R560–R573.
- Cole, D.G., Reedy, M.V., 2003. Algal Morphogenesis: How *Volvox* turns itself inside-out. *Curr. Biol.* 13 (19), R770–R772.
- Danas, K., Reis, P.M., 2024. Stretch-independent magnetization in incompressible isotropic hard magnetorheological elastomers. *J. Mech. Phys. Solids* 191, 105764.
- Dorfmann, A., Ogden, R.W., 2004. Nonlinear magnetoelastic deformations of elastomers. *Acta Mech.* 167 (1–2), 13–28.
- Dorfmann, L., Ogden, R.W., 2024. Hard-magnetic soft magnetoelastic materials: Energy considerations. *Int. J. Solids Struct.* 294, 112789.
- Du, Y., Su, Y., Lü, C., Chen, W., Destrade, M., 2020. Electro-mechanically guided growth and patterns. *J. Mech. Phys. Solids* 143 (2), 104073.
- Firouzi, N., Amabili, M., 2024. Two-dimensional growth of incompressible and compressible soft biological tissues. *Eur. J. Mech. A Solids* 103, 105150.
- Franze, K., 2020. Integrating chemistry and mechanics: The forces driving axon growth. *Annu. Rev. Cell. Dev. Biol.* 36, 61–83.
- Garcia-Gonzalez, D., Hossain, M., 2021. Microstructural modelling of hard-magnetic soft materials: dipole-dipole interactions versus Zeeman effect. *Extrem. Mech. Lett.* 48, 101382.
- Gomez-Cruz, C., Fernandez-de la Torre, M., Lachowski, D., Prados-de-Haro, M., del Río Hernández, A.E., Perea, G., Muñoz-Barrutia, A., Garcia-Gonzalez, D., 2024. Mechanical and functional responses in astrocytes under alternating deformation modes using magneto-active substrates. *Adv. Mater.* 36 (26), 2312497.
- Goriely, A., 2017. The Mathematics and Mechanics of Biological Growth, vol. 45, Springer.
- Goriely, A., Ben Amar, M., 2005. Differential growth and instability in elastic shells. *Phys. Rev. Lett.* 94 (19), 198103.
- Haas, P.A., Goldstein, R.E., 2015. Elasticity and gloability: initiation of embryonic inversion in *Volvox*. *J. R. Soc. Interface* 12 (112), 20150671.
- Himpel, G., Kuhl, E., Menzel, A., Steinmann, P., 2005. Computational modelling of isotropic multiplicative growth. *Comput. Model. Eng. Sci.* 8 (2), 119–134.
- Hiraki, H.L., Matera, D.L., Rose, M.J., Kent, R.N., Todd, C.W., Stout, M.E., Wank, A.E., Schiavone, M.C., DePalma, S.J., Zarouk, A.A., Baker, B.M., 2021. Magnetic alignment of electrospun fiber segments within a hydrogel composite guides cell spreading and migration phenotype switching. *Front. Bioeng. Biotechnol.* 9, 679165.
- Höhn, S., Honerkamp-Smith, A.R., Haas, P.A., Trong, P.K., Goldstein, R.E., 2015. Dynamics of a *Volvox* embryo turning itself inside out. *Phys. Rev. Lett.* 114 (17), 178101.
- Hong, W., Zhao, X., Zhou, J., Suo, Z., 2008. A theory of coupled diffusion and large deformation in polymeric gels. *J. Mech. Phys. Solids* 56 (5), 1779–1793.
- Hossain, M., Steinmann, P., 2013. More hyperelastic models for rubber-like materials: Consistent tangent operators and comparative study. *J. Mech. Behav. Mater.* 22 (1–2), 27–50.
- Hu, J., Li, H., Du, J., Liu, Z., Carrera, E., 2024. Inhomogeneous large deformation of magneto-thermal sensitive hydrogel-based composite structures. *Mech. Adv. Mater. Struct.* 31 (1), 138–146.
- Kadapa, C., Hossain, M., 2022. A linearized consistent mixed displacement-pressure formulation for hyperelasticity. *Mech. Adv. Mater. Struct.* 29 (2), 267–284.
- Kadapa, C., Li, Z., Hossain, M., Wang, J., 2021. On the advantages of mixed formulation and higher-order elements for computational morphoelasticity. *J. Mech. Phys. Solids* 148, 104289.
- Khalid, M.Y., Arif, Z.U., Tariq, A., Hossain, M., Ahmed Khan, K., Umer, R., 2024. 3D printing of magneto-active smart materials for advanced actuators and soft robotics applications. *Eur. Polym. J.* 205, 112718.
- Kim, Y., Yuk, H., Zhao, R., Chester, S.A., Zhao, X., 2018. Printing ferromagnetic domains for untethered fast-transforming soft materials. *Nature* 558 (7709), 274–279.
- Kobayashi, K., Yoon, C., Oh, S.H., Pagaduan, J.V., Gracias, D.H., 2019. Biodegradable thermomagnetically responsive soft untethered grippers. *ACS Appl. Mater. Interfaces* 11 (1), 151–159.
- Kondraurov, V., Nikitin, L., 1987. Finite strains of viscoelastic muscle tissue. *J. Appl. Math. Mech.* 51 (3), 346–353.
- Lee, Y.W., Kim, J.K., Bozuyuk, U., Dogan, N.O., Khan, M.T.A., Shiva, A., Wild, A.M., Sitti, M., 2023. Multifunctional 3D-printed pollen grain-inspired hydrogel microrobots for on-demand anchoring and cargo delivery. *Adv. Mater.* 35 (10), 2209812.
- Li, C., Armstrong, J.P., Pence, I.J., Kit-Anan, W., Puetzer, J.L., Correia Carreira, S., Moore, A.C., Stevens, M.M., 2018. Glycosylated superparamagnetic nanoparticle gradients for osteochondral tissue engineering. *Biomaterials* 176, 24–33.
- Li, B., Cao, Y.P., Feng, X.Q., Gao, H., 2012. Mechanics of morphological instabilities and surface wrinkling in soft materials: A review. *Soft Matter* 8 (21), 5728.
- Li, Y., Huang, G., Zhang, X., Li, B., Chen, Y., Lu, T., Lu, T.J., Xu, F., 2013. Magnetic hydrogels and their potential biomedical applications. *Adv. Funct. Mater.* 23 (6), 660–672.
- Li, Z., Kadapa, C., Hossain, M., Wang, J., 2023a. A numerical framework for the simulation of coupled electromechanical growth. *Comput. Methods Appl. Mech. Engrg.* 414, 116128.
- Li, Z., Wang, J., Hossain, M., Kadapa, C., 2023b. A general theoretical scheme for shape-programming of incompressible hyperelastic shells through differential growth. *Int. J. Solids Struct.* 265–266, 112128.
- Liu, C., Du, Y., Li, K., Han, Z., Lü, C., 2024a. Growth and morphogenesis of an everted tubular biological tissue. *Proc. R. Soc. A: Math. Phys. Eng. Sci.* 480 (2283), 20230816.
- Liu, C., Wang, F., Tao, W., Lü, C., 2024b. Geometrical incompatibility regulated pattern selection and morphological evolution in growing spherical soft tissues. *Int. J. Mech. Sci.* 284, 109720.
- Lu, L., Sim, J., Zhao, R.R., 2024. Mechanics of hard-magnetic soft materials: A review. *Mech. Mater.* 189, 104874.
- Matt, G., Umen, J., 2016. Volvox: A simple algal model for embryogenesis, morphogenesis and cellular differentiation. *Dev. Biol.* 419 (1), 99–113.
- Mihai, L.A., Budday, S., Holzapfel, G.A., Kuhl, E., Goriely, A., 2017. A family of hyperelastic models for human brain tissue. *J. Mech. Phys. Solids* 106, 60–79.
- Moreno-Mateos, M.A., Danas, K., Garcia-Gonzalez, D., 2023. Influence of magnetic boundary conditions on the quantitative modelling of magnetorheological elastomers. *Mech. Mater.* 184, 104742.
- Moreno-Mateos, M.A., Hossain, M., Steinmann, P., Garcia-Gonzalez, D., 2023. Hard magnetics in ultra-soft magnetorheological elastomers enhance fracture toughness and delay crack propagation. *J. Mech. Phys. Solids* 173, 105232.
- Mukherjee, D., Rambausek, M., Danas, K., 2021. An explicit dissipative model for isotropic hard magnetorheological elastomers. *J. Mech. Phys. Solids* 151, 104361.
- Nemer, R., Larcher, A., Coupez, T., Hachem, E., 2021. Stabilized finite element method for incompressible solid dynamics using an updated Lagrangian formulation. *Comput. Methods Appl. Mech. Engrg.* 384, 113923.
- Ogden, R., 1997. Non-linear elastic deformations. In: Dover Civil and Mechanical Engineering. Dover Publications.

- Pelteret, J.P., Davydov, D., McBride, A., Vu, D.K., Steinmann, P., 2016. Computational electro-elasticity and magneto-elasticity for quasi-incompressible media immersed in free space. *Internat. J. Numer. Methods Engrg.* 108 (11), 1307–1342.
- Rahmati, A.H., Jia, R., Tan, K., Zhao, X., Deng, Q., Liu, L., Sharma, P., 2023. Theory of hard magnetic soft materials to create magnetoelectricity. *J. Mech. Phys. Solids* 171, 105136.
- Rambausek, M., Mukherjee, D., Danas, K., 2022. A computational framework for magnetically hard and soft viscoelastic magnetorheological elastomers. *Comput. Methods Appl. Mech. Engrg.* 391, 114500.
- Rausch, M.K., Kuhl, E., 2014. On the mechanics of growing thin biological membranes. *J. Mech. Phys. Solids* 63, 128–140.
- Reese, S., Küssner, M., Reddy, B.D., 1999. A new stabilization technique for finite elements in non-linear elasticity. *Internat. J. Numer. Methods Engrg.* 44 (11), 1617–1652.
- Rodríguez, E.K., Hoger, A., McCulloch, A.D., 1994. Stress-dependent finite growth in soft elastic tissues. *J. Biomech.* 27 (4), 455–467.
- Sadik, S., Yavari, A., 2017. On the origins of the idea of the multiplicative decomposition of the deformation gradient. *Math. Mech. Solids* 22 (4), 771–772.
- Skalak, R., Zargaryan, S., Jain, R.K., Netti, P.A., Hoger, A., 1996. Compatibility and the genesis of residual stress by volumetric growth. *J. Math. Biol.* 34 (8), 889–914.
- Tang, J., Yin, Q., Qiao, Y., Wang, T., 2019. Shape morphing of hydrogels in alternating magnetic field. *ACS Appl. Mater. Interfaces* 11 (23), 21194–21200.
- Toupin, R., 1956. The elastic dielectric. *J. Ration. Mech. Anal.* 5 (6), 849–915.
- van Rees, W.M., Vouga, E., Mahadevan, L., 2017. Growth patterns for shape-shifting elastic bilayers. *Proc. Natl. Acad. Sci.* 114 (44), 11597–11602.
- Vítková, L., Kazantseva, N., Musilová, L., Smolka, P., Valášková, K., Kocourková, K., Humeník, M., Minařík, A., Humpolíček, P., Mráček, A., Smolková, I., 2023. Magneto-responsive hyaluronan hydrogel for hyperthermia and bioprinting: Magnetic, rheological properties and biocompatibility. *APL Bioeng.* 7 (3), 036113.
- Wang, Z., Li, Z., Wang, J., 2025. Asymptotic analyses on field-induced bending deformations of multi-layered hard-magnetic soft material plates. *Int. J. Solids Struct.* 310, 113217.
- Wang, J., Zeng, J., Wang, Z., Du, P., 2024. A finite-strain plate model for the magneto-mechanical behaviors of hard-magnetic soft material plates. *Appl. Math. Model.* 134, 223–248.
- Wang, J., Zhang, H., Zheng, Y., Ye, H., 2020. High-order NURBS elements based isogeometric formulation for swellable soft materials. *Comput. Methods Appl. Mech. Engrg.* 363, 112901.
- Xue, S.L., Li, B., Feng, X.Q., Gao, H., 2016. Biochemomechanical poroelastic theory of avascular tumor growth. *J. Mech. Phys. Solids* 94, 409–432.
- Yan, D., Aymon, B.F.G., Reis, P.M., 2023. A reduced-order, rotation-based model for thin hard-magnetic plates. *J. Mech. Phys. Solids* 170, 105095.
- Yavari, A., 2010. A geometric theory of growth mechanics. *J. Nonlinear Sci.* 20 (6), 781–830.
- Yu, X., Chen, X., 2024. An asymptotically consistent morphoelastic shell model for compressible biological structures with finite-strain deformations. *J. Mech. Phys. Solids* 191, 105768.
- Zhao, R., Kim, Y., Chester, S.A., Sharma, P., Zhao, X., 2019. Mechanics of hard-magnetic soft materials. *J. Mech. Phys. Solids* 124, 244–263.